FORMACION PLANETARIA

Curso Planetología 2014

www.astronomia.edu.uy/depto/planetologia/planet.html

Tabaré Gallardo

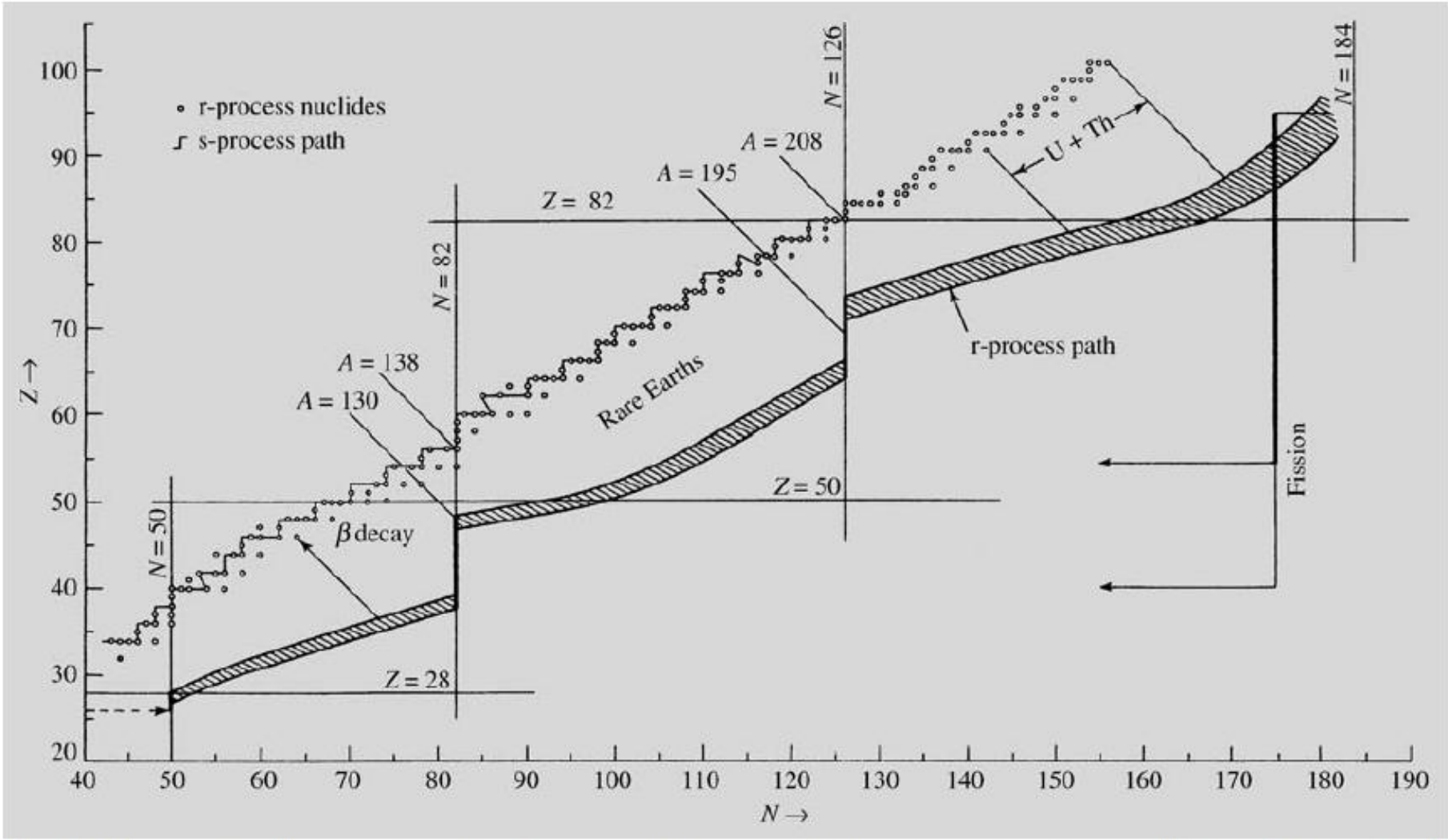

Fig. 11.14. Neutron capture paths for the s-process and r-process (*from left to right*). The s-process follows a path along the line of beta stability. The stable r-process nuclei (*small circles*) result from beta decay of their neutron rich progenitors on the shaded path shown lower. Beta decay occurs along straight lines $A = \text{const}$. The closed neutron shells in nuclei at $N = 50$, 82 and 126 correspond to abundance peaks in s-process nuclei at $A = 88$, 138 and 208, and in r-process nuclei at $A = 80$, 130 and 195. (Seeger, P.A., Fowler, W.A., Clayton, D.D. (1965): Astrophys. J. Suppl. **11**, 121)

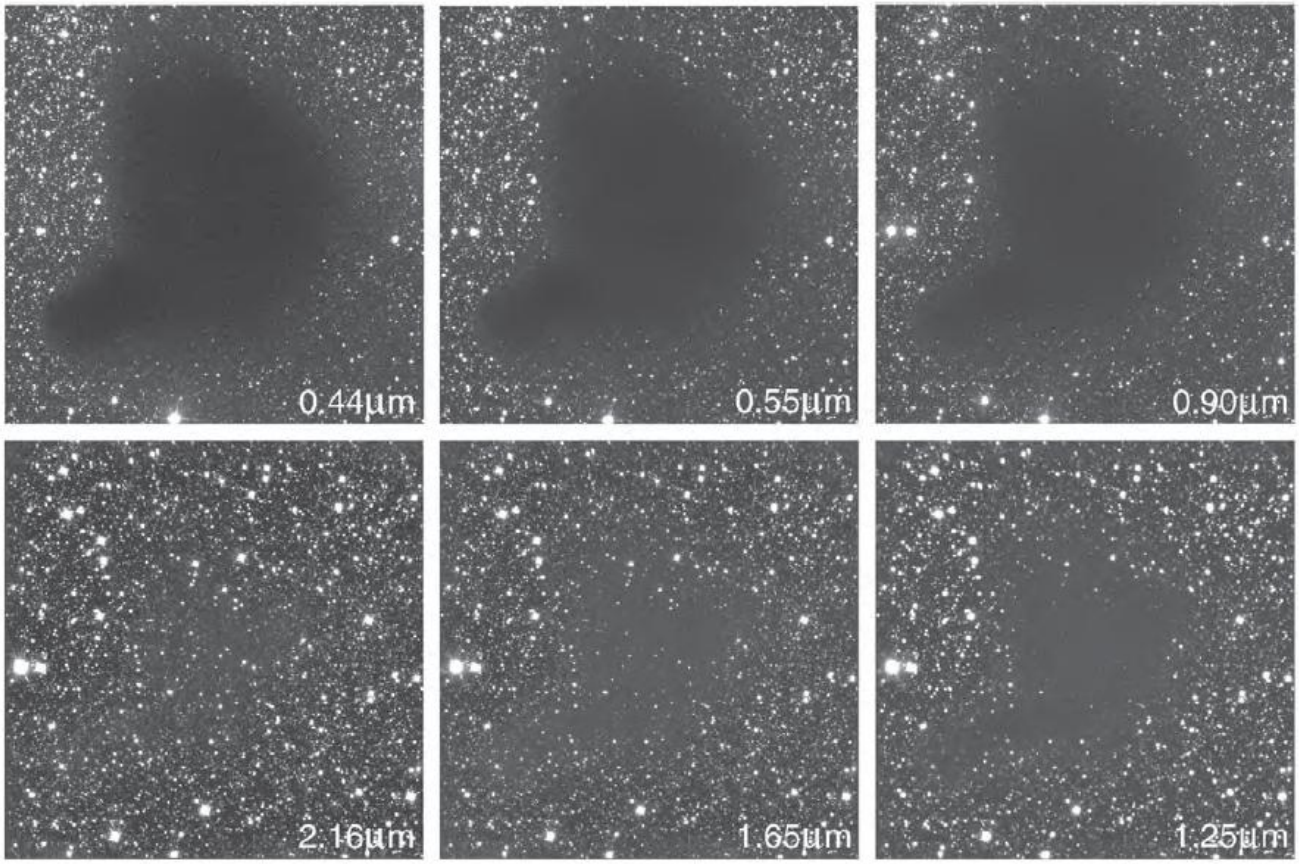

Figure 15.1 The sky area of the globule Barnard 68 in the Ophiuchus star-forming region, imaged in six different wavebands, clockwise from the blue to the near-infrared spectral region. The obscuration caused by the cloud diminishes dramatically with increasing wavelength, implying that most of the dust is in the form of sub-μm grains. Because the outer regions of the cloud are less dense than the inner ones, the apparent size of the cloud also decreases as wavelength increases, with more background stars shining through the outer parts. (European Southern Observatory PR Photo 29b/99)

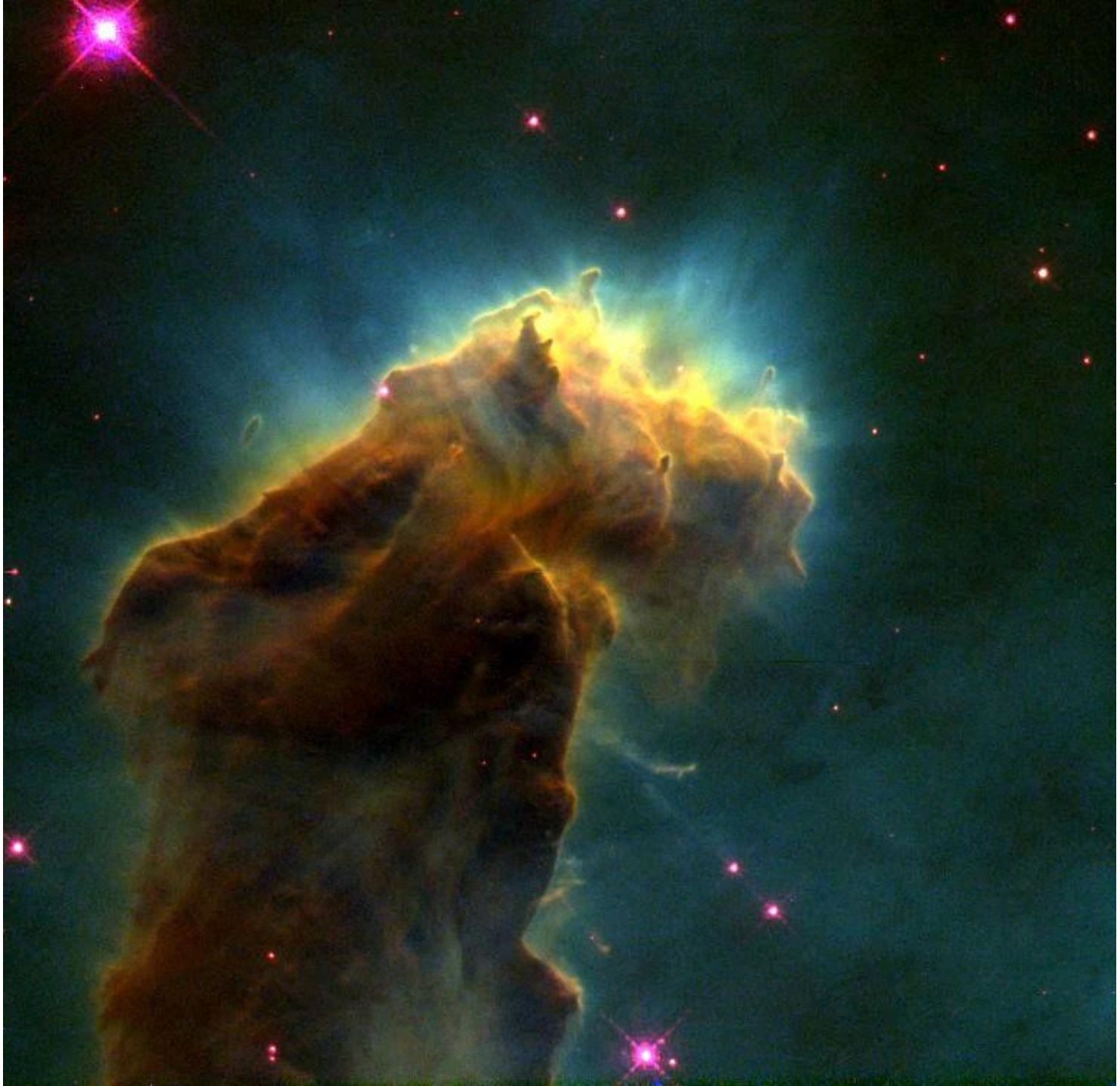

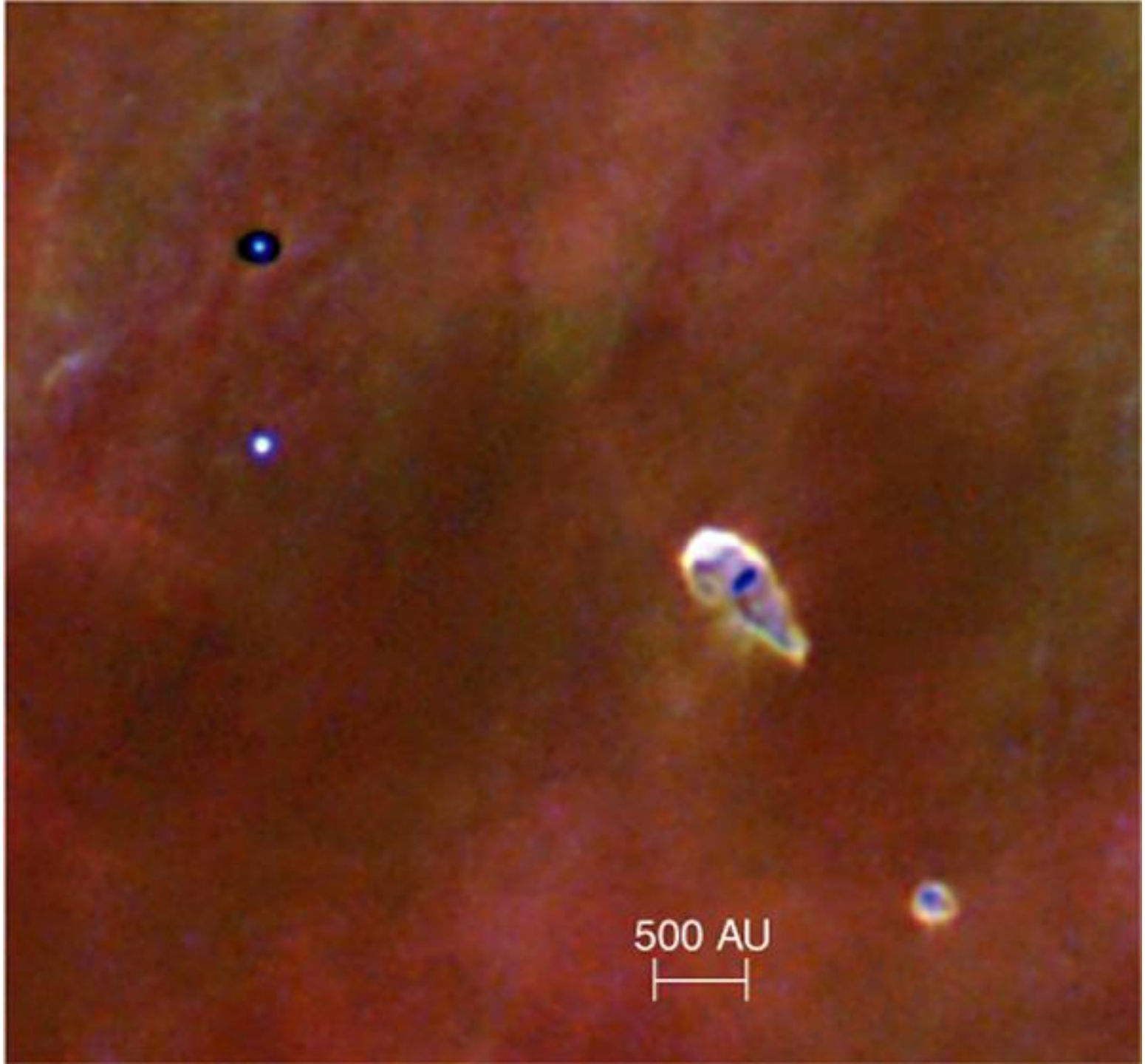
500 AU

Fig. 5.3 A diagram illustrating star formation. The star forms following the collapse of a rotating cloud of interstellar material, which flattens into a disk, perpendicular to its rotation axis. The stellar wind, which is confined by the magnetic field, escapes in two lobes that are aligned with the rotation axis (After Acker, 2005)

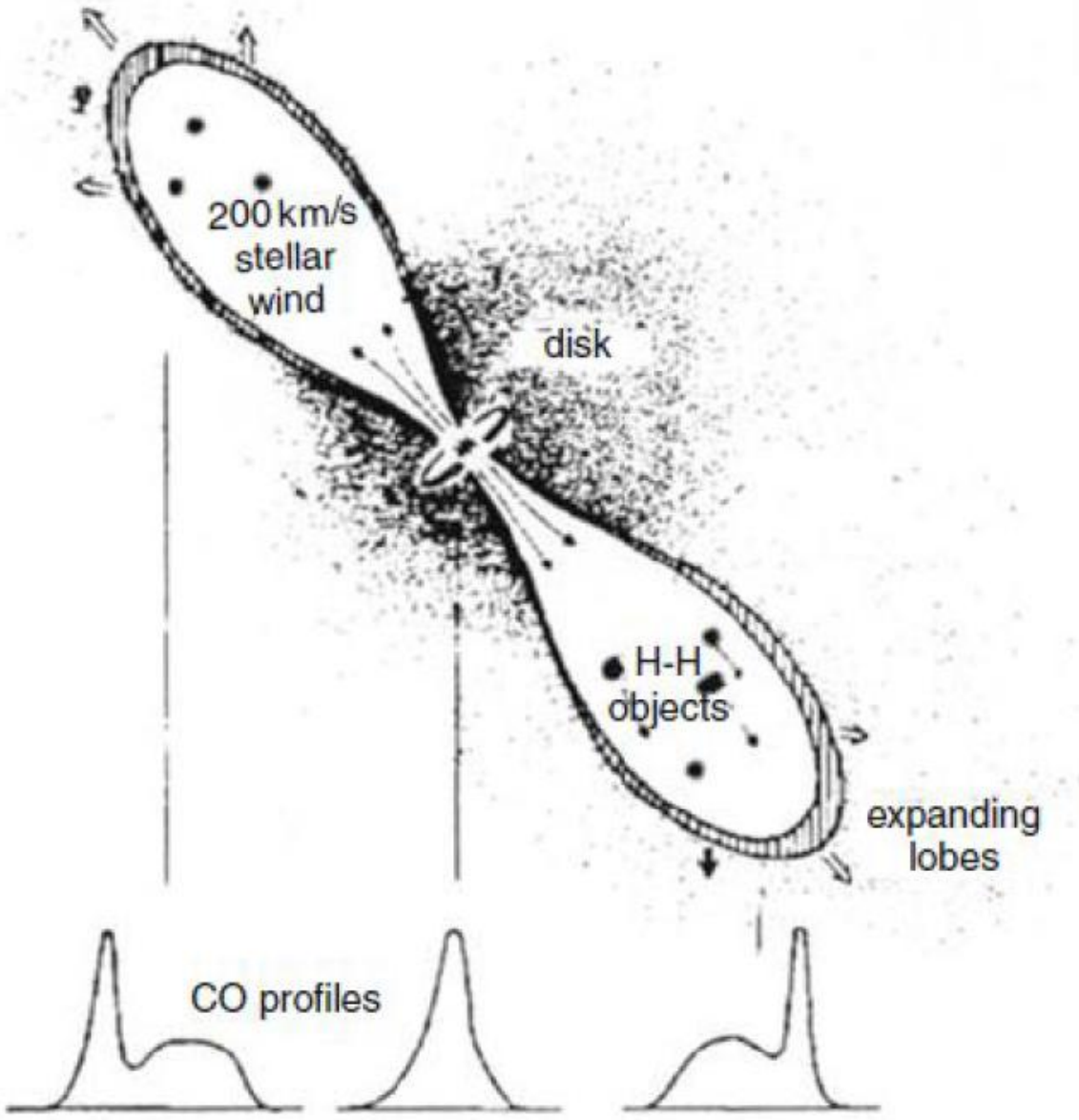

Snell 1980

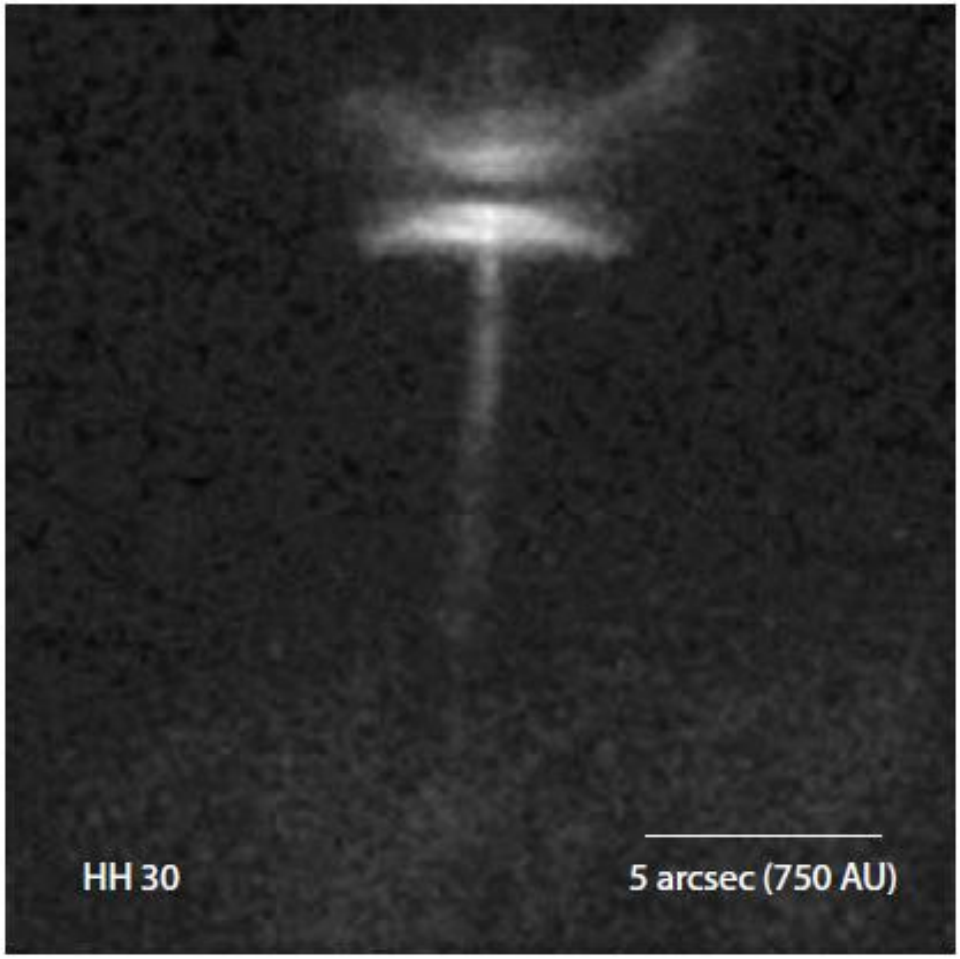

Figure 10.2: The Herbig–Haro object HH30, at a distance of ~150 pc, observed by HST. Two thin jets flow outwards from the young stellar object in the centre. The two lenticular regions are scattered light from dust in the disk. The dark central lane is the accretion disk observed edge-on (courtesy NASA/ESA/STScI).

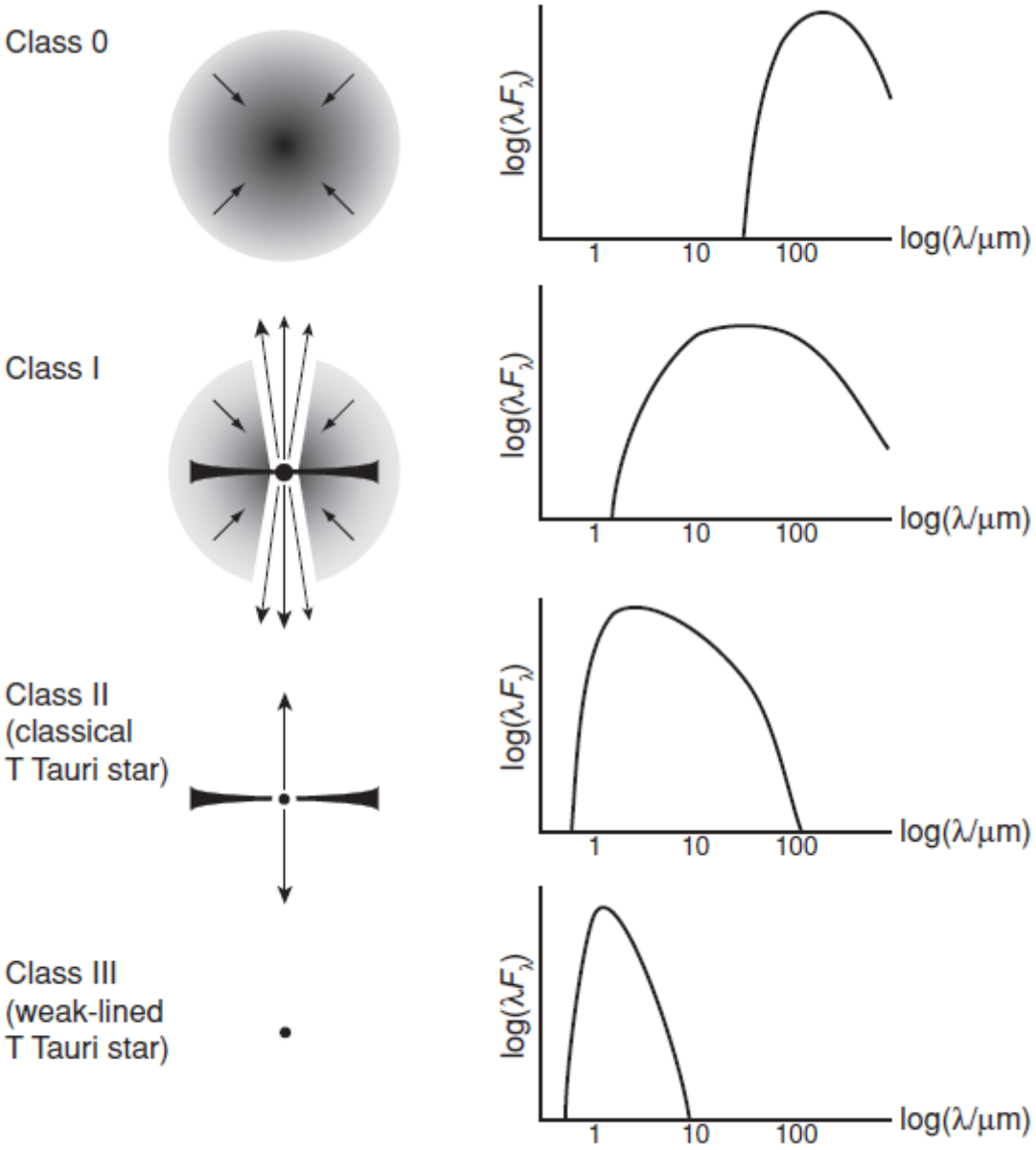

Fig. 2.1. Classification scheme for Young Stellar Objects.

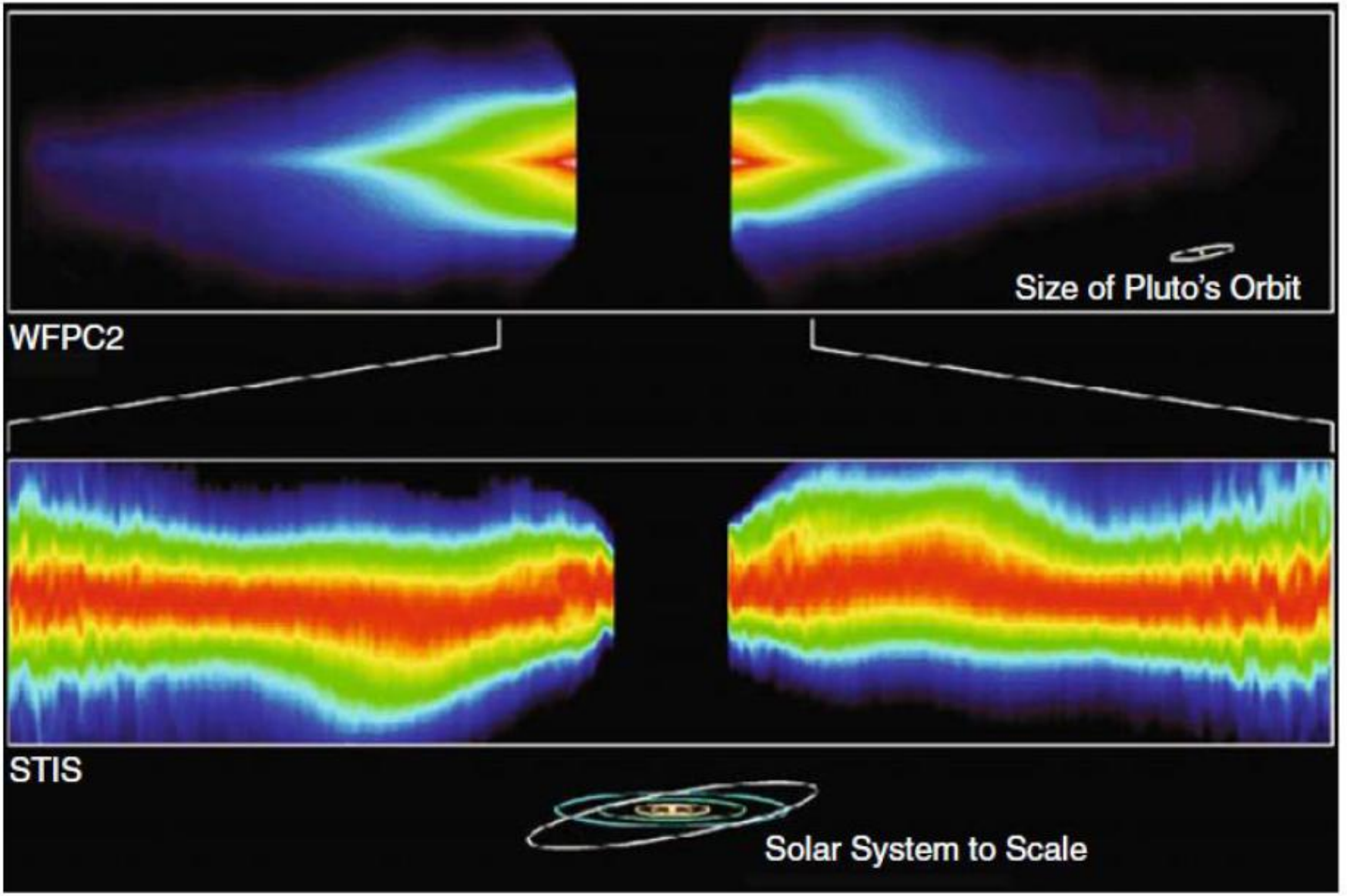

Fig. 5.22 Coronographic images of the disk of β Pic obtained with the STIS instrument on the HST. *Top*: overall image; *bottom*: enlargement of the central portion, with a vertical exaggeration of 4 times, to reveal the warping of the disk. The intensity (and thus the quantity of dust) is a maximum near the equatorial plane (After Heap et al., 2000)

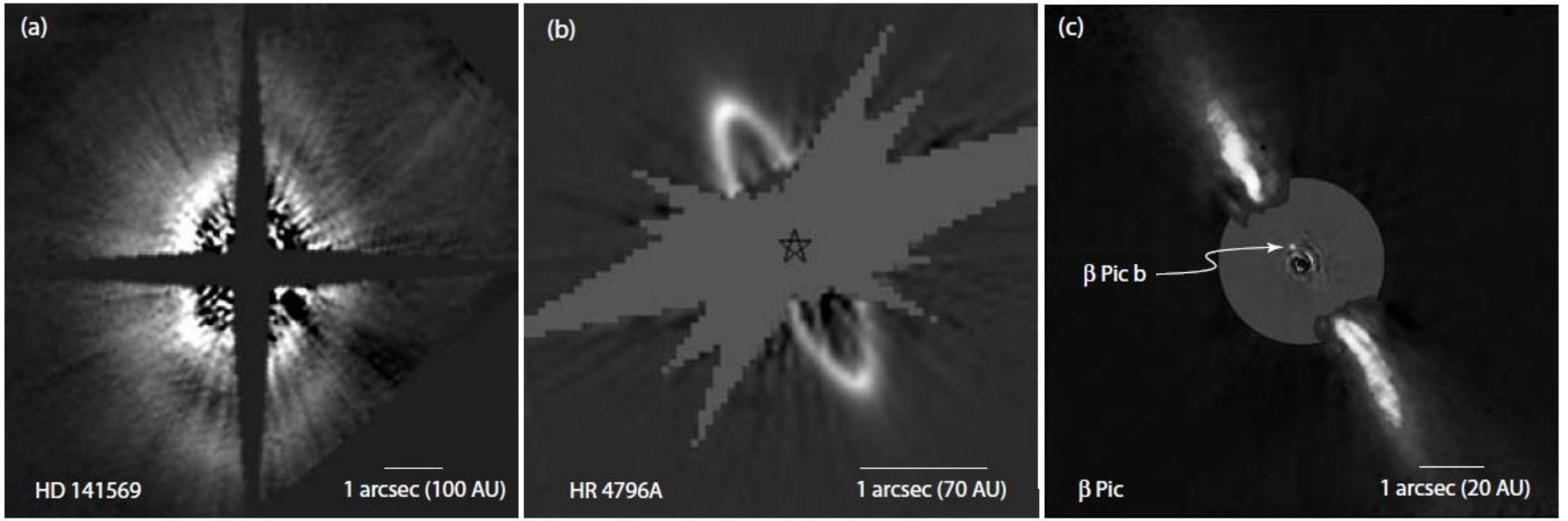

Figure 10.4: Examples of imaged debris disks: (a) HD 141569 observed at 1.1 μm with HST–NICMOS (Weinberger et al., 1999, Figure 1). (b) HR 4796A, observed in the optical with HST–STIS (Schneider et al., 2009a, Figure 2; this version courtesy G. Schneider). (c) β Pic, from combined ESO 3.6-m ADONIS imaging in 1996 (outer region), and 3.6 μm observations with VLT–NACO (inner region) revealing the probably planet, β Pic b (Lagrange et al., 2009b, this version courtesy A.M. Lagrange, D. Ehrenreich, and ESO). In all cases, the geometric central structures are artefacts of the coronagraphic imaging.

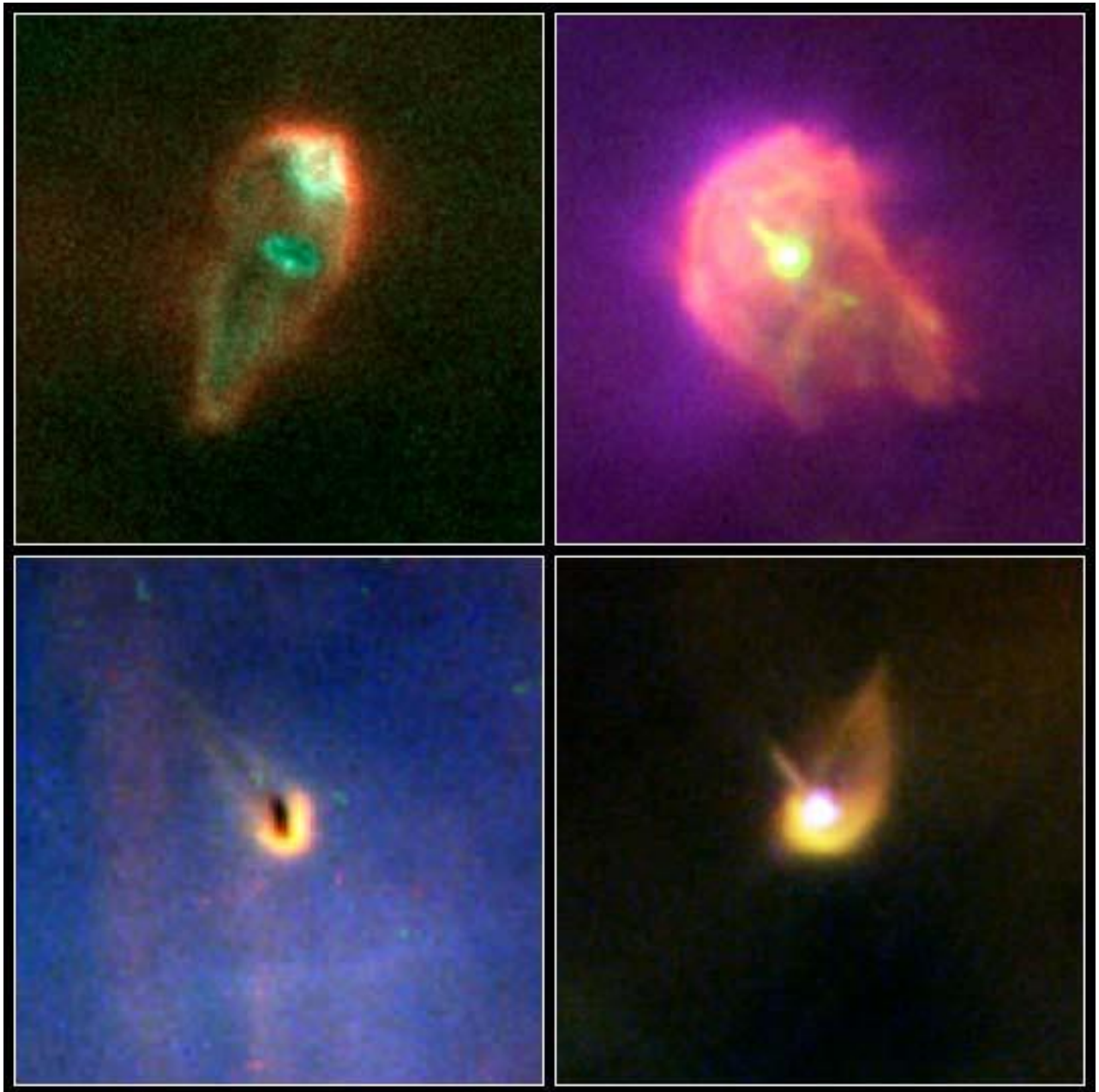

Protoplanetary Disks in the Orion Nebula **HST** • WFPC2

NASA, J. Bally (University of Colorado), H. Throop (SWRI),
and C.R. O'Dell (Vanderbilt University) • STScI-PRC01-13

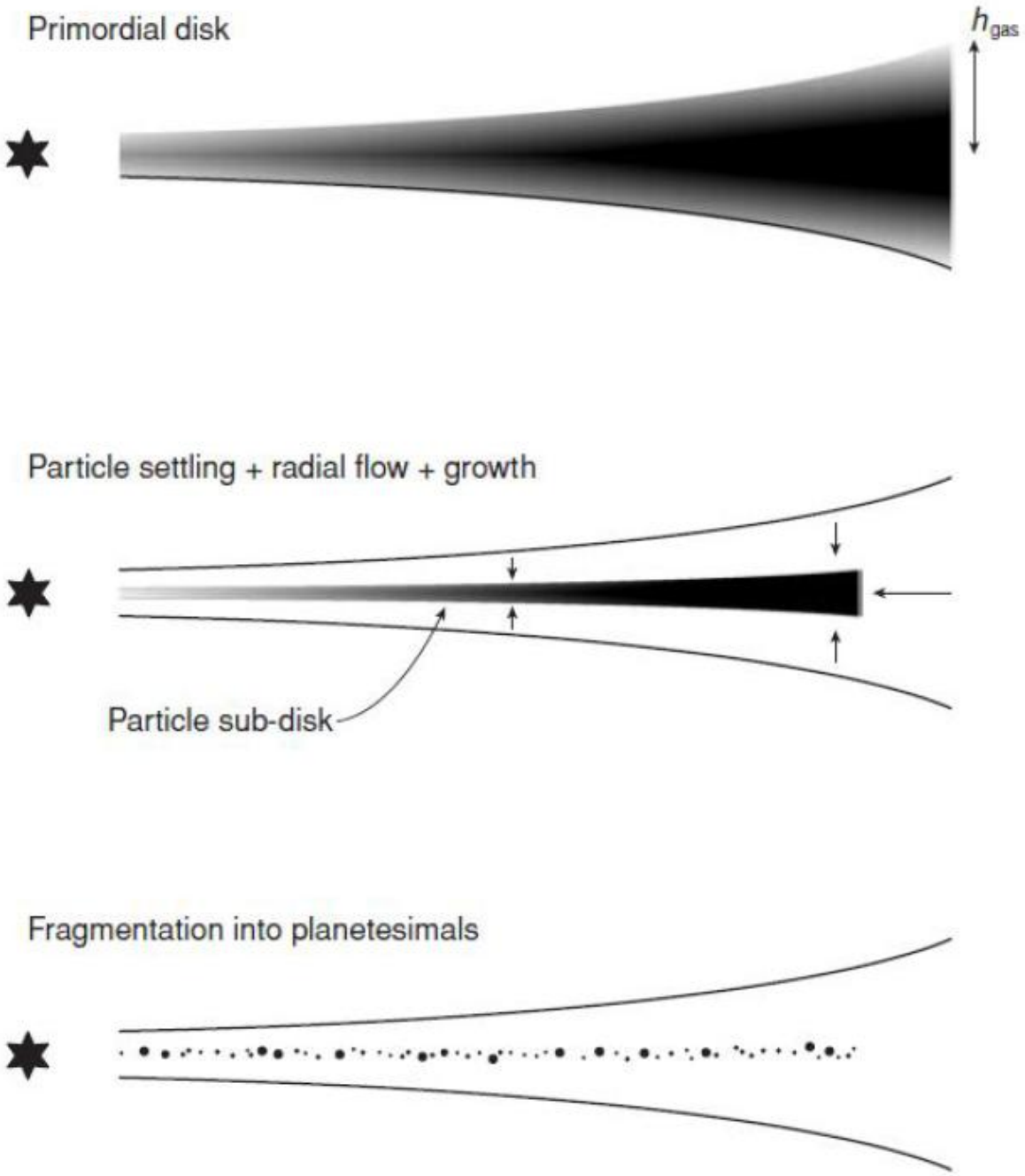

Fig. 4.7. How planetesimals form within the classical Goldreich–Ward scenario.

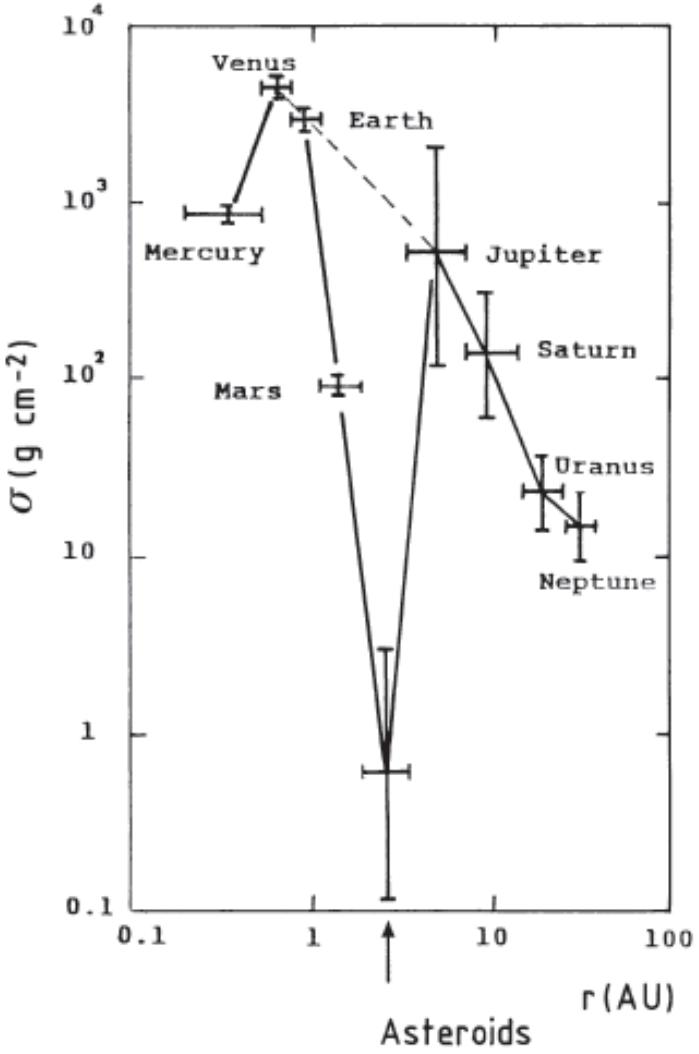

Fig. 16.1. The surface density of the primordial solar nebula vs. heliocentric distance, obtained by restoring the planets to solar composition and spreading the resulting masses through contiguous zones surrounding the present orbits. The zone boundaries are taken as the arithmetic means of adjacent orbits (for Mercury and Neptune, the zones are assumed to cover equal distances inward and outward from their orbits). The horizontal bars in the figure show the resulting zone widths, and the vertical error bars reflect the estimated uncertainties in planetary compositions. For the asteroids, an original mass ranging between the present mass (= 5.10^{-4} $M_\oplus$) and 25 times this value has been assumed. (Figure adopted from Weidenschilling (1977)).

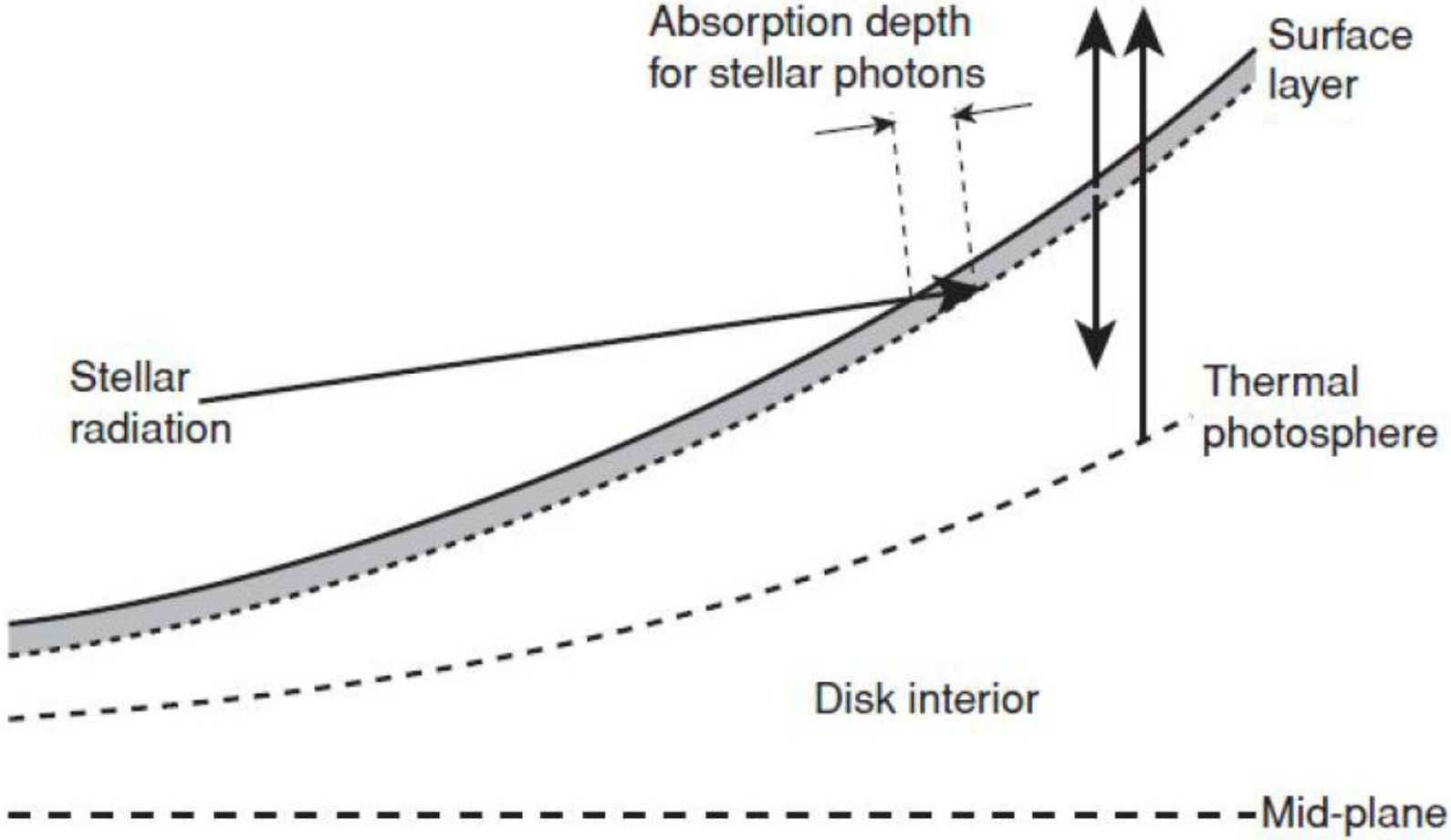

Fig. 2.5. The physics underlying radiative equilibrium models for protoplanetary disks. Stellar radiation is absorbed in a thin surface layer by dust, which reradiates in the infrared both upward into space and downward where it is absorbed once more and acts to heat the disk interior. The local emission from the disk is a superposition of radiation from the hot surface layer and the cooler interior.

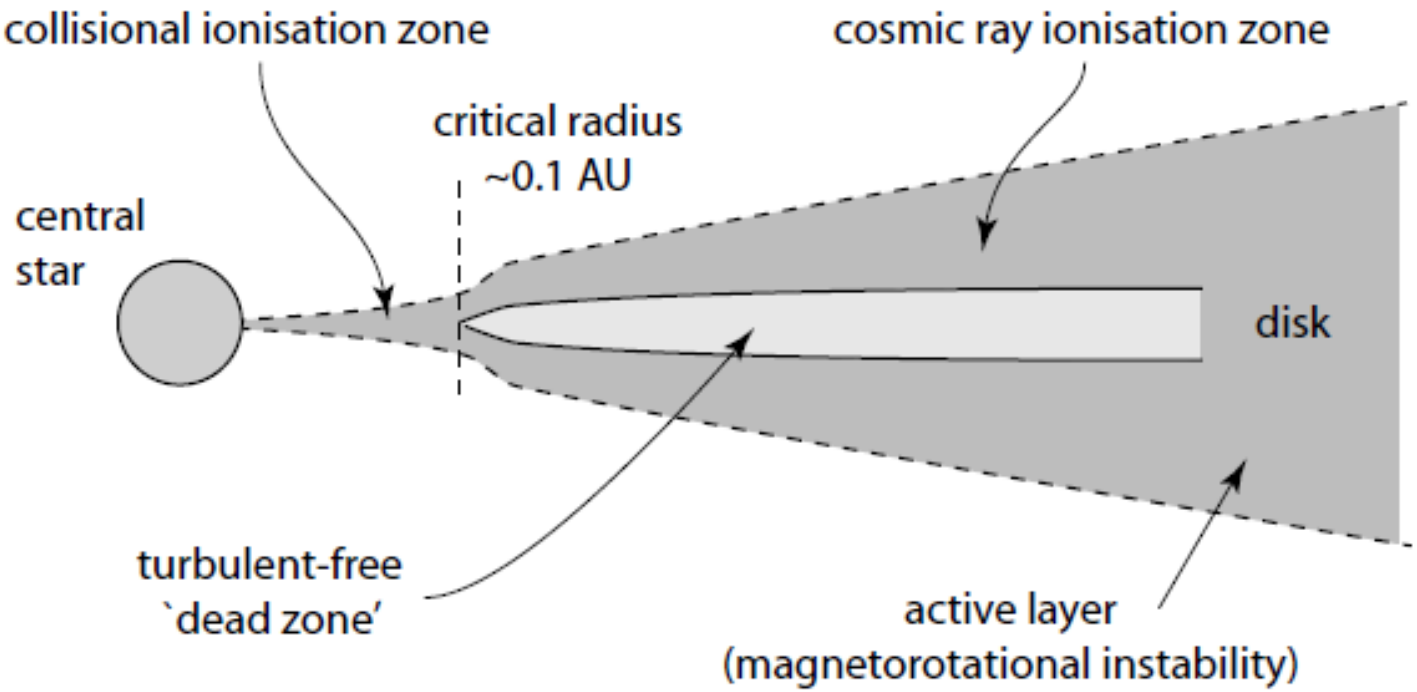

Figure 10.3: Schematic of a layered accretion disk. Inside 0.1 AU, where $T \sim 10^3$ K, collisional ionisation ensures magnetorotational instability, and enables accretion. At large radii, cosmic rays penetrate the entire disk. At intermediate radii, they ionise a layer of thickness $\sim 10^3$ kg m^{-2} on either side. Between the active layers is a 'dead zone' where turbulence and accretion are inhibited. Adapted from Gammie (1996, Figure 1).

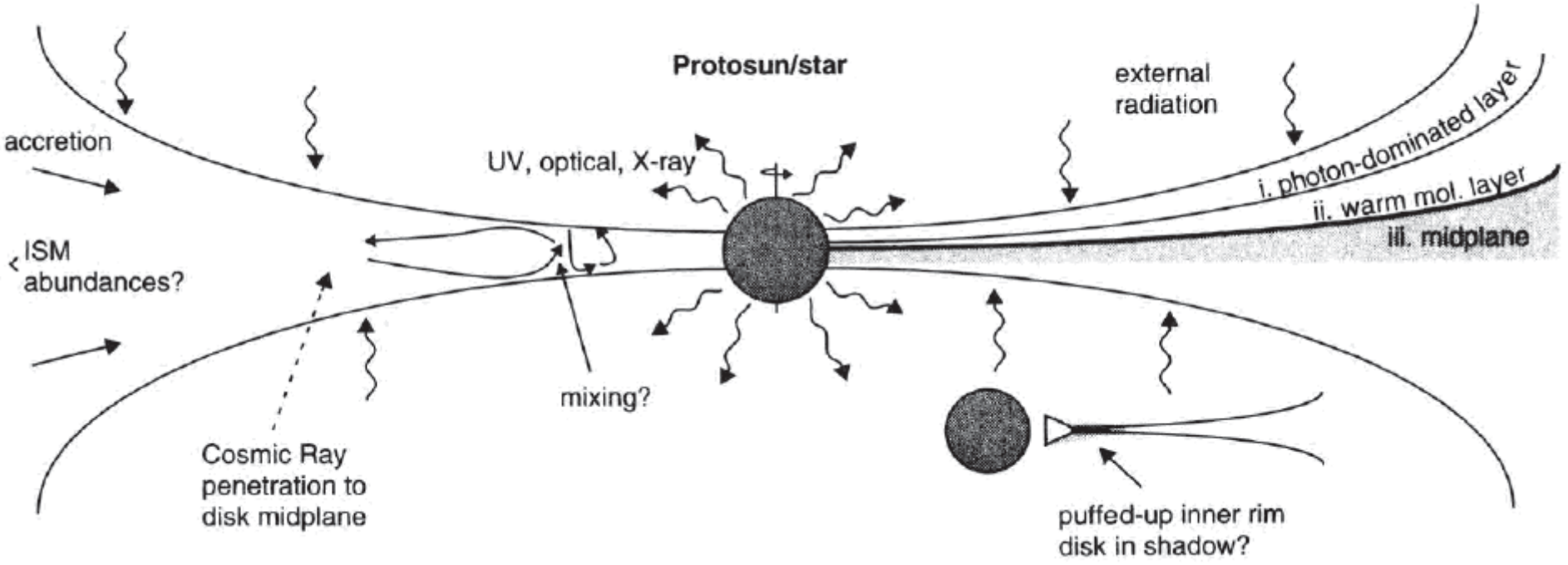
Protosun/star
external
radiation
accretion
UV, optical, X-ray
i. photon-dominated layer
ii. warm mol. layer
iii. midplane
ISM
abundances?
mixing?
Cosmic Ray
penetration to
disk midplane
puffed-up inner rim
disk in shadow?

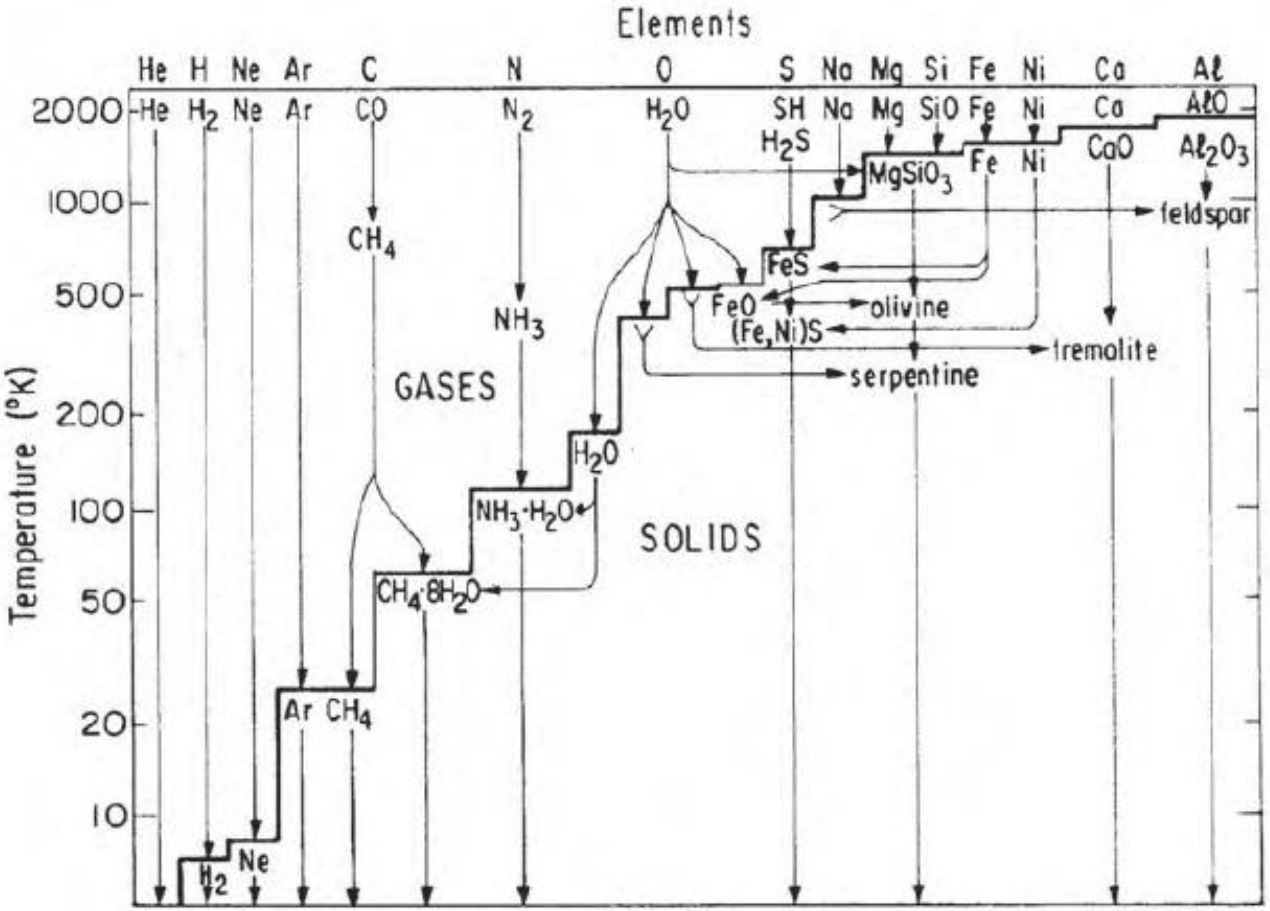

Figure 15.5 Flow chart of major reactions during fully equilibrated cooling of solar nebula material from 2000 to 5 K. The fifteen most abundant elements are listed across the top, and directly beneath are the dominant gas species of each element at 2000 K. The staircase curve separates gases from condensed phases. (Barshay and Lewis 1976)

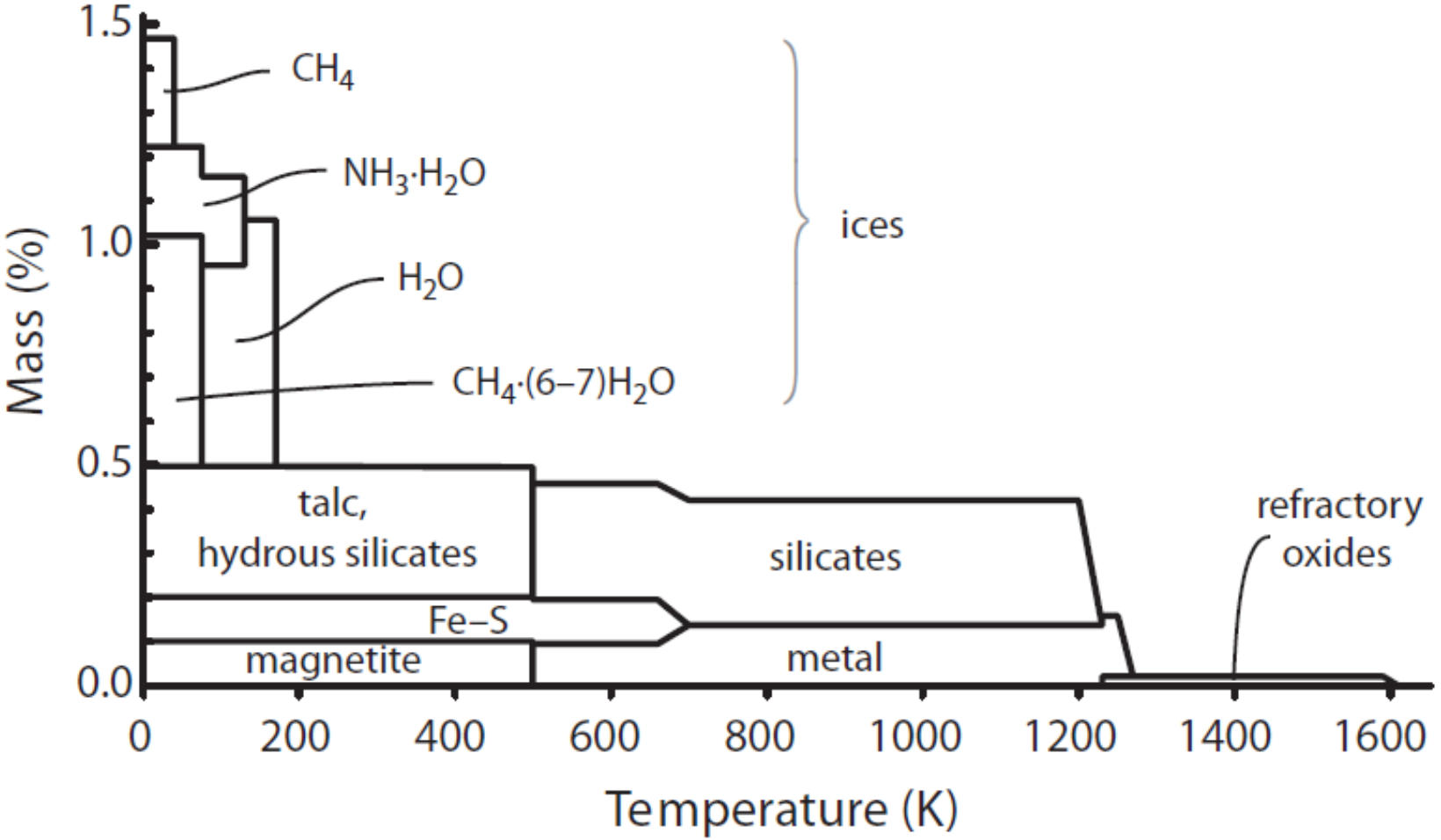

Figure 15.6 Amount and composition of major condensed components formed during fully equilibrated cooling of solar nebula material. (Lodders 2010)

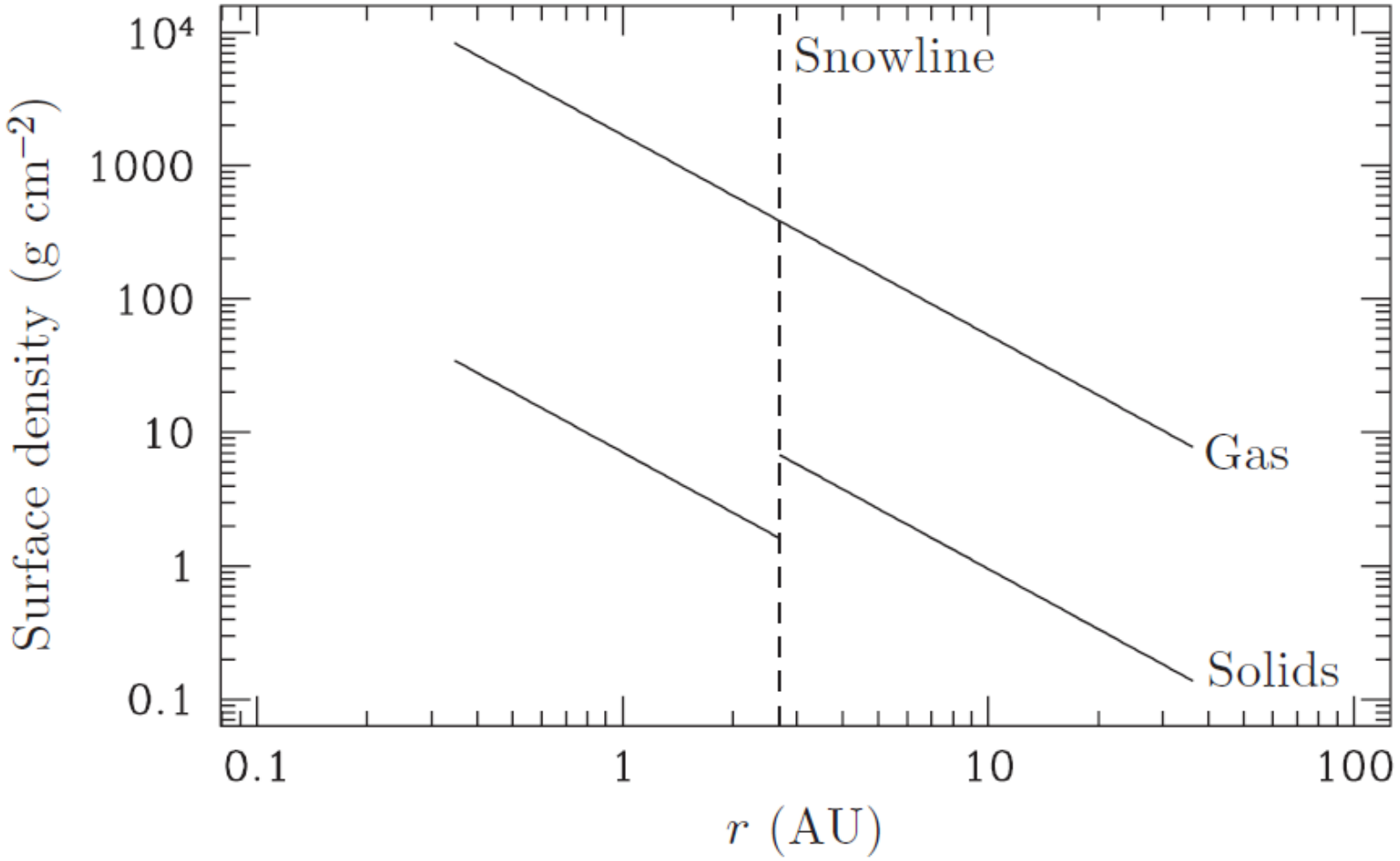

Fig. 1.1. The surface density in gas (upper line) and solids (lower broken line) as a function of radius in Hayashi's minimum mass Solar Nebula. The dashed vertical line denotes the location of the snowline.

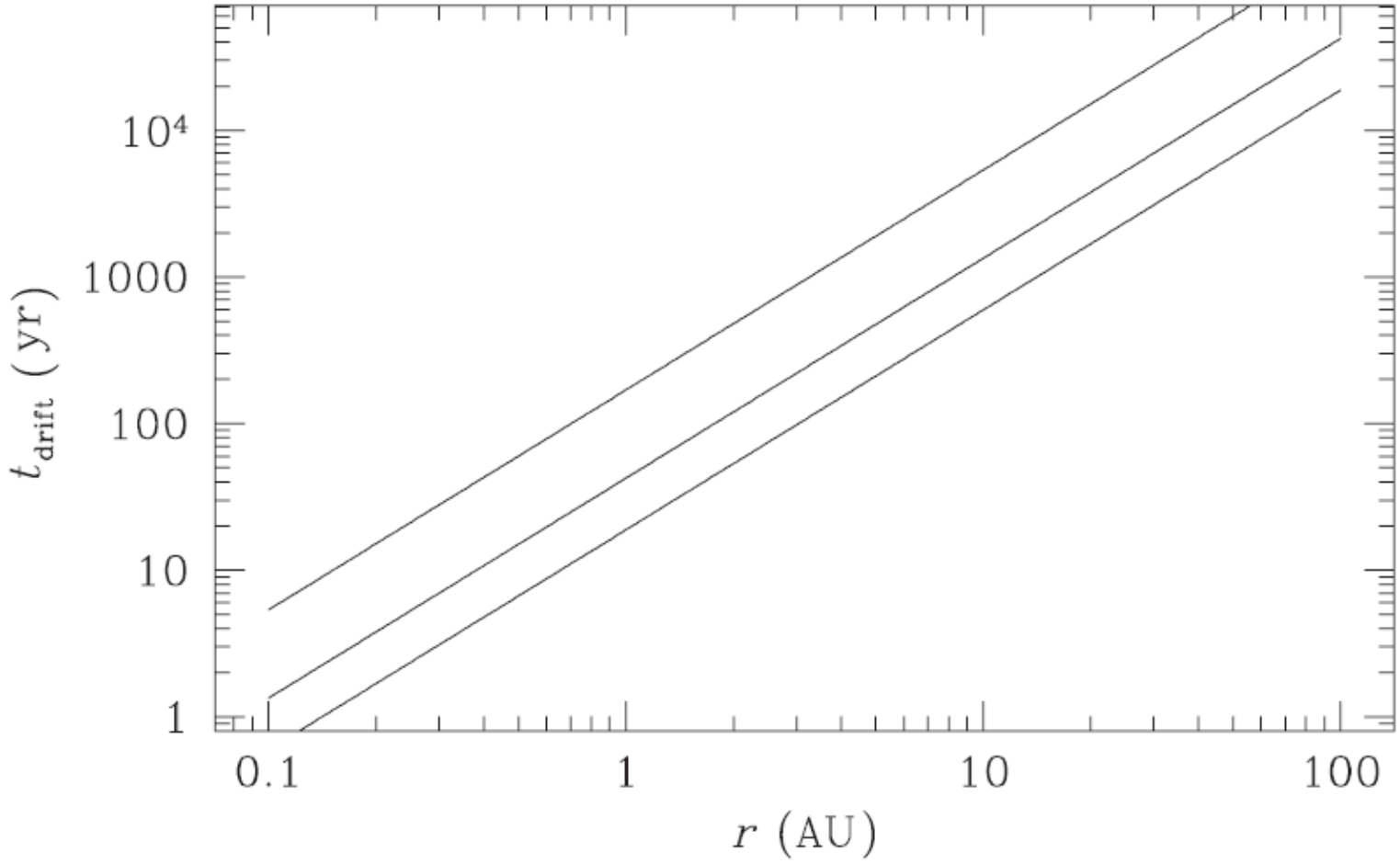

Fig. 4.3. The *minimum* time scale for the radial drift of solid particles as a function of radius, for disk models in which $\Sigma \propto r^{-1}$ and $h/r = 0.025$ (uppermost line), $h/r = 0.05$, or $h/r = 0.075$ (bottom line).

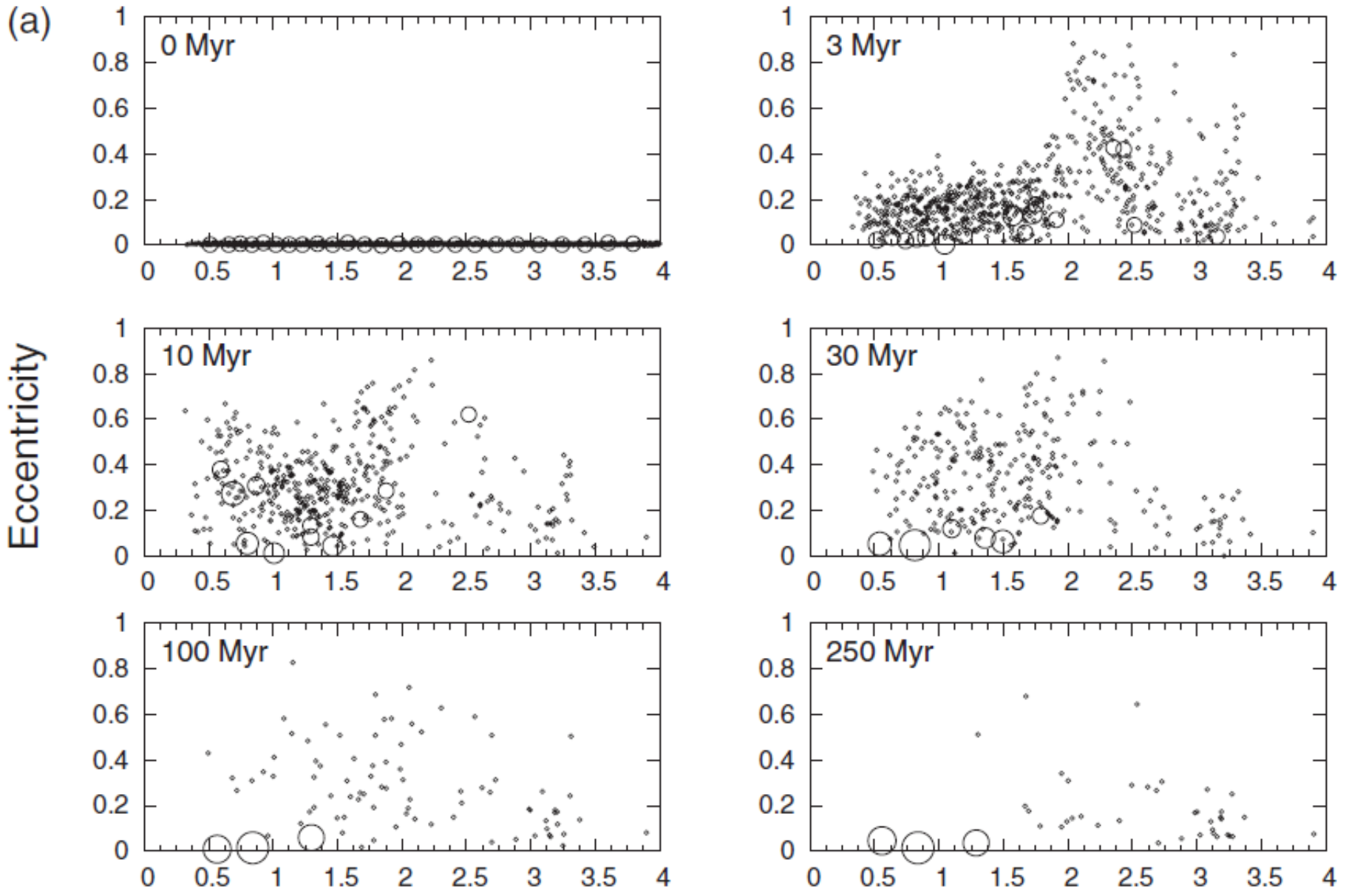
(a)
0 Myr
3 Myr
10 Myr
30 Myr
100 Myr
250 Myr
Eccentricity
Semimajor Axis (AU)
0
0.2
0.4
0.6
0.8
1
0
0.5
1
1.5
2
2.5
3
3.5
4

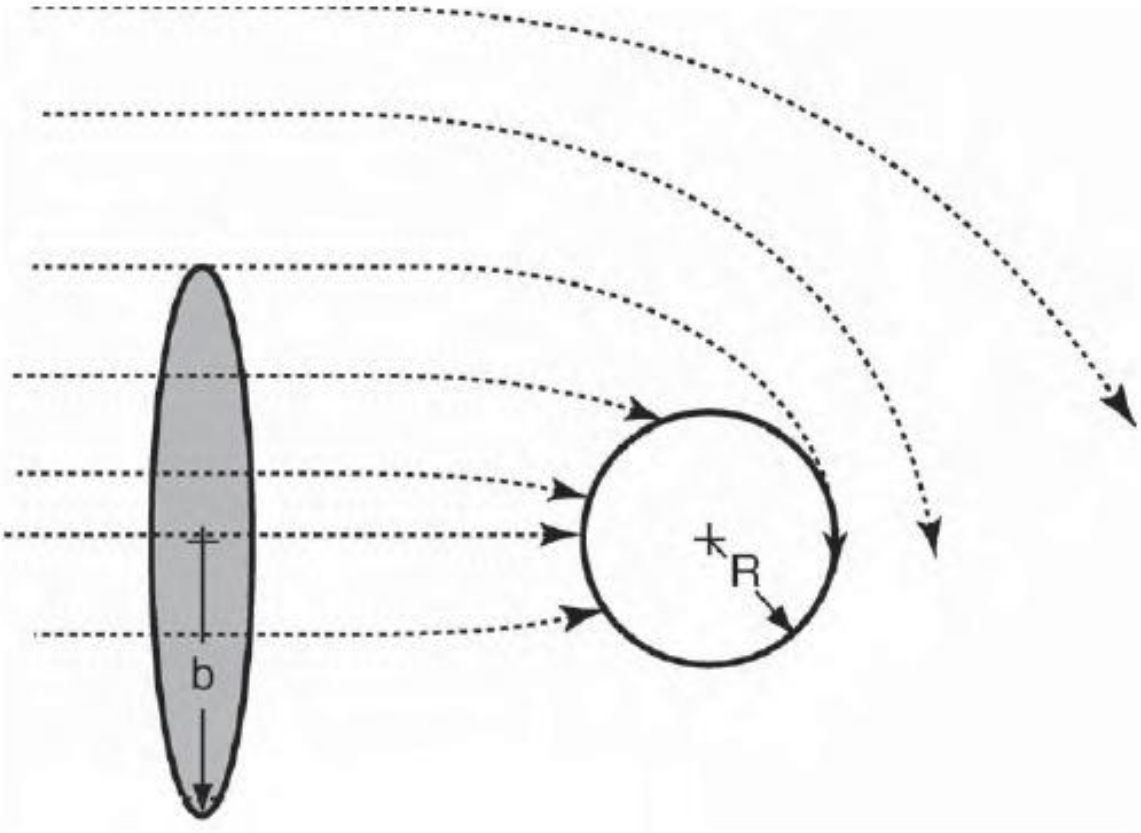

Figure 15.7 Schematic diagram of the gravitational focusing of planetesimal trajectories by an accreting planetary embryo or planet. The critical trajectory that collides tangentially with the planet has an **unperturbed impact parameter**, b, larger than the radius of the planet, $b > R$. (Adapted from Brownlee and Kress 2007)

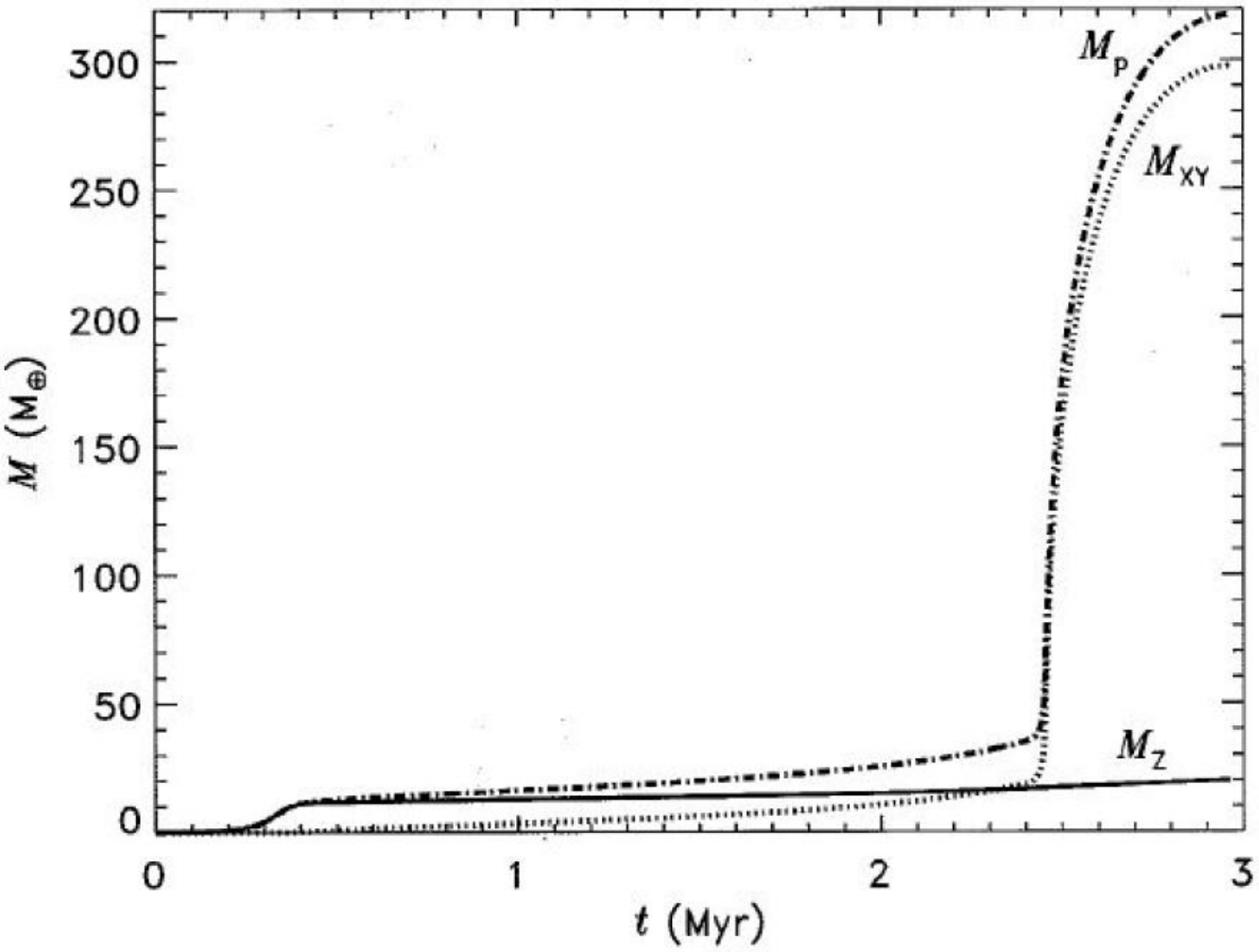

Figure 13.22 The mass of a giant planet that grows to 1 M_J is shown as a function of time according to one particular simulation based upon the core nucleated accretion model. The planet's total mass is represented by the dot-dashed curve, the mass of the solid component is given by the solid curve, and the dotted curve represents the gas mass. The solid core grows rapidly by runaway accretion in the first 4×10^5 years. The rate of solid body accumulation decreases once the planet has accreted nearly all of the condensed material within its gravitational reach. The envelope accumulates gradually, with its settling rate determined by its ability to radiate away the energy of accretion. Eventually, the planet becomes sufficiently cool and massive that gas can be accreted rapidly. This simulation is for growth at 5.2 AU from a 1 $M_\odot$ star, with a local surface mass density of solids equal to 10 g/cm^2. (Lissauer *et al.* 2009)

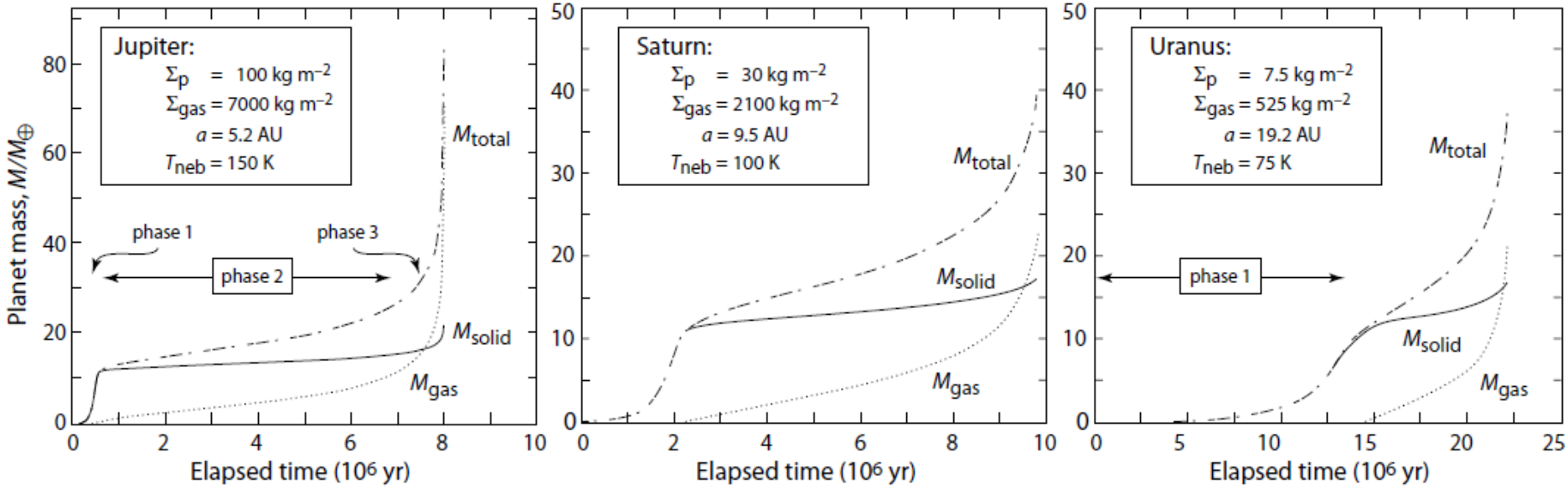

Figure 10.11: Giant planet formation by core accretion. Simulations correspond to the cases of Jupiter, Saturn, and Uranus (models J1, S1, and U1 from Table III of Pollack et al. 1996). Values shown are the initial conditions for the planetesimal and gas surface densities Σ_p and Σ_{gas}, the initial embryo semi-major axis a, and nebula temperature T_{neb}. Simulations begin with an embryo mass comparable to that of Mars, with almost all its mass in a high-Z core. Planetesimals have a radius of 100 km. The results show, as a function of time, the total planet mass M_{total}, and the corresponding contributions from accumulated solids M_{solid}, and accumulated gas M_{gas} (dashed, solid, and dotted lines respectively). From Pollack et al. (1996, Figures 1, 4, 5).

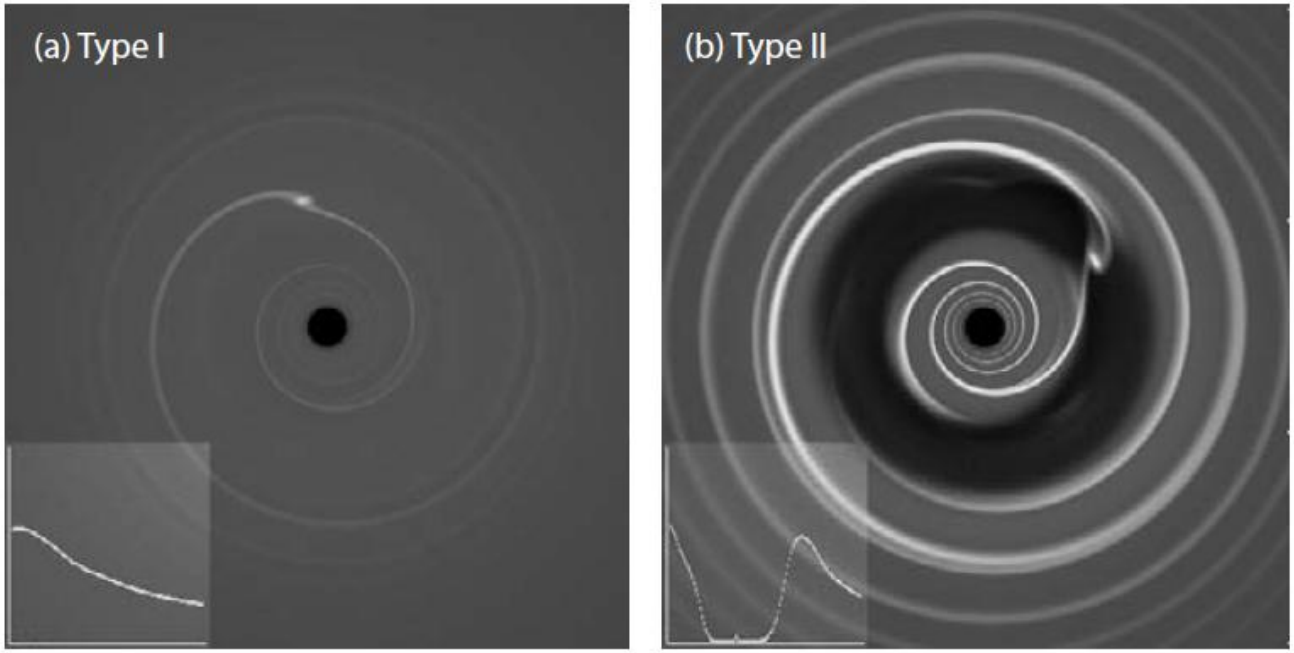

Figure 10.14: Type I and type II migration. Simulations of the interaction between a planet on a circular orbit with a laminar (non-turbulent) protoplanetary disk, computed from a two-dimensional isothermal hydrodynamic code with a constant kinematic viscosity: (a) in type I migration, a relatively low-mass planet excites a wave in the gas disk, but does not significantly perturb the azimuthally-averaged surface density profile (inset); (b) in type II migration, a more massive planet (here of $10 M_{\rm J}$) clears an annular gap, within which the surface density is a small fraction of its unperturbed value. As the disk evolves, the planet follows the motion of the gas (either inward or outward) while remaining within the gap. From Armitage & Rice (2005, Figure 1).

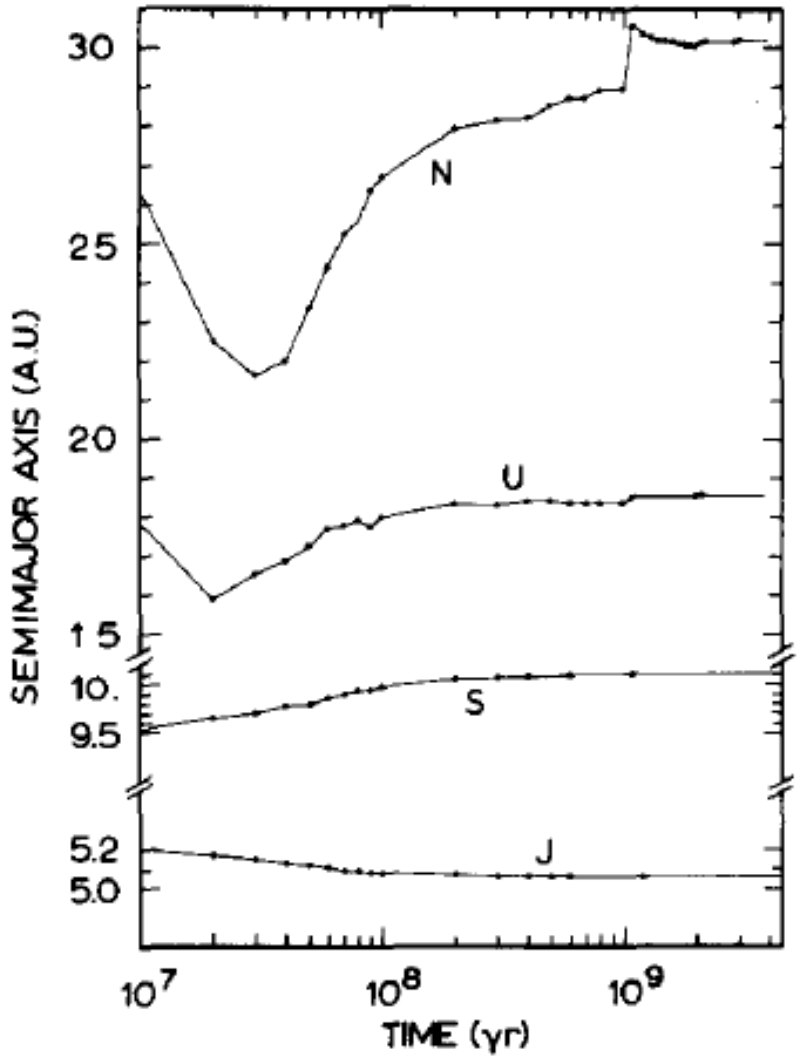

FIG. 3. Time variation of the semimajor axes of the four Jovian planets as a result of exchange of angular momentum with planetesimals. These results are taken from case 7. The initial semimajor axes are a_J = 5.203 AU, a_S = 9.54 AU, a_U = 20 AU and a_N = 30 AU.

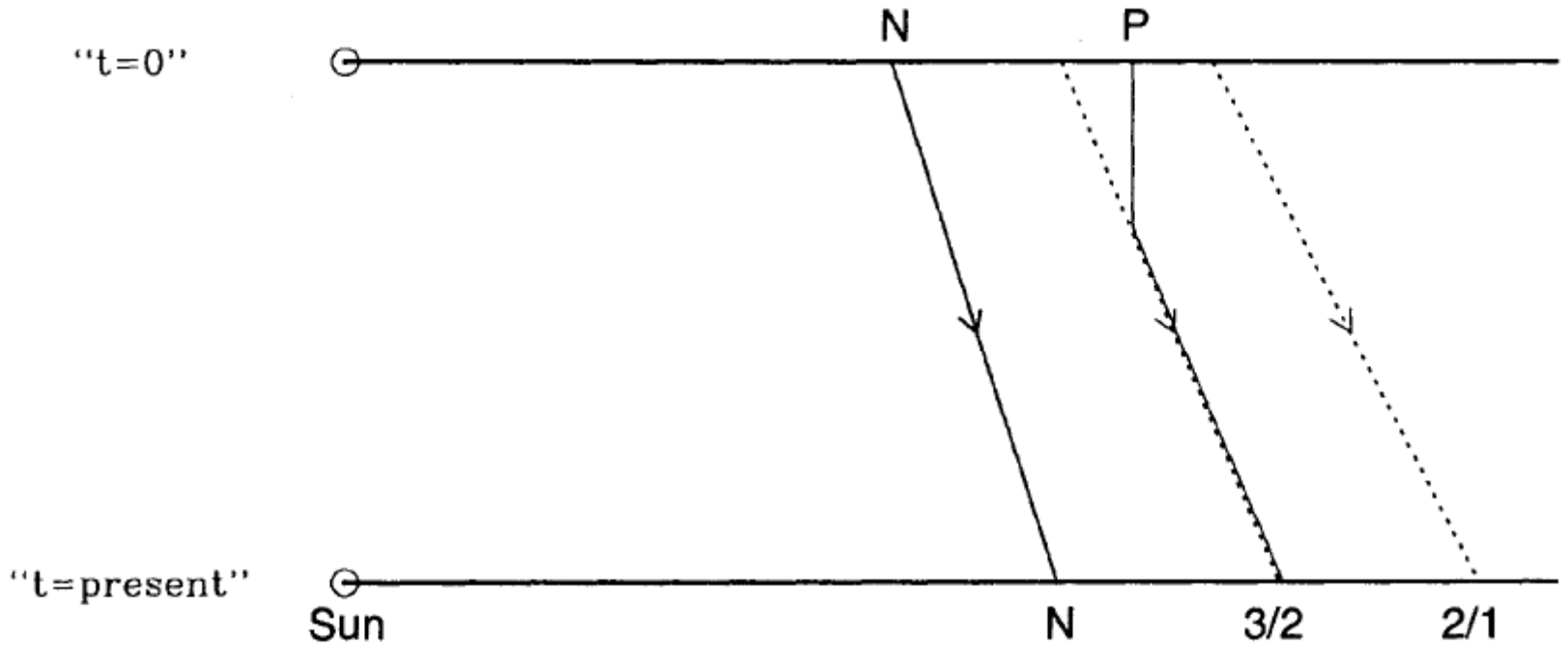

FIG. 1. A schematic diagram to illustrate the outward radial migration of Neptune and its exterior orbital resonances during the late stages of planet formation. The distance from the Sun is along the horizontal direction. Neptune's outward orbital migration is shown along the path marked N–N. For clarity, only two first-order resonances (3:2 and 2:1) are shown (dotted lines). A "Pluto" in an initially circular, nonresonant orbit beyond Neptune could have been captured into the 3:2 resonance and would evolve along the solid line path indicated by P—3/2.

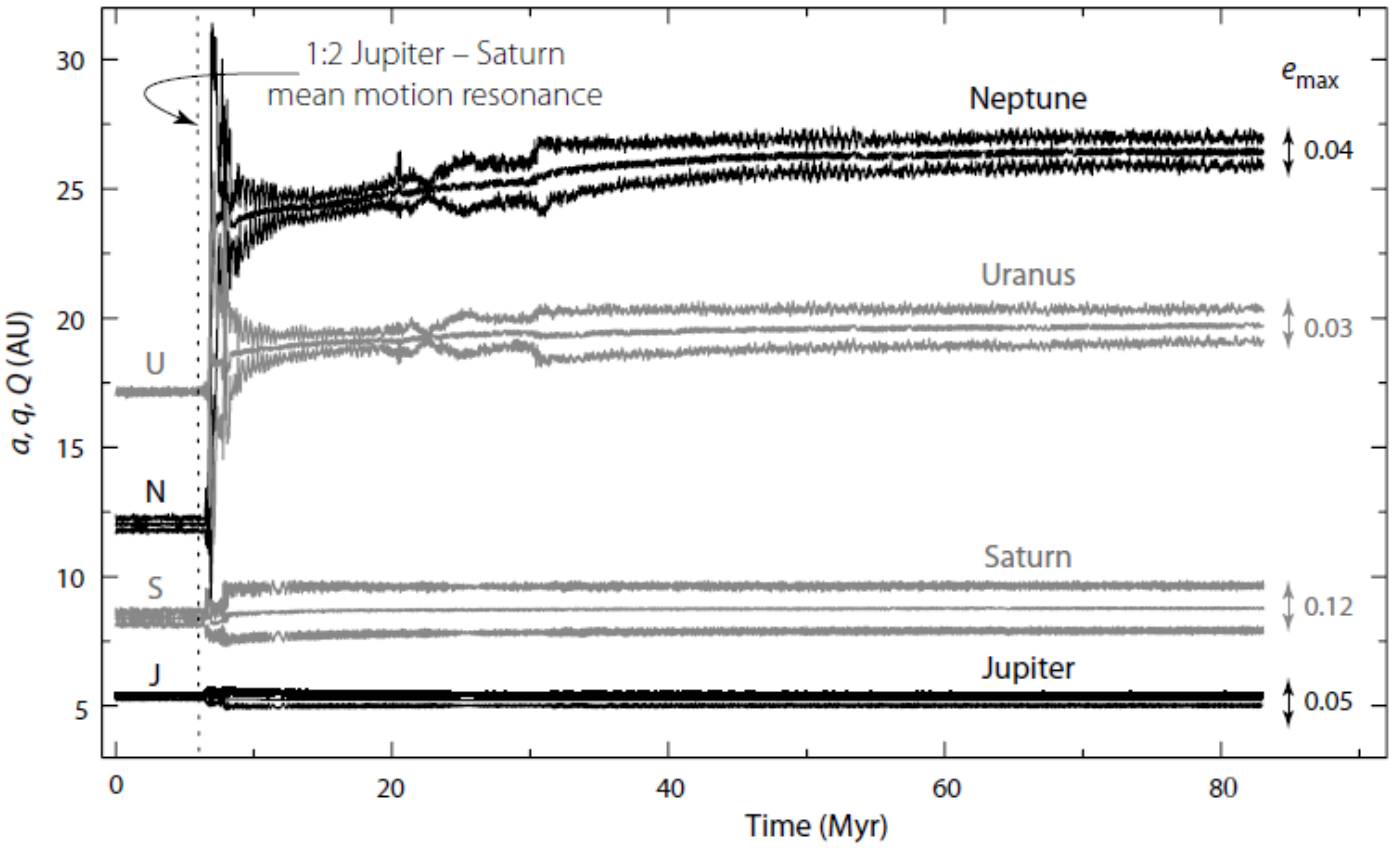

Figure 12.4: The starting configuration of the outer solar system planets given by the Nice model, with their subsequent orbital evolution from an N-body simulation with $35 M_{\oplus}$ of disk planetesimals in 3500 particles out to 30 AU. The three curves for each planet indicate the semi-major axis a, and their minimum (q) and maximum (Q) heliocentric distances. The vertical dashed line marks the epoch of the 1:2 Jupiter–Saturn mean motion resonance capture. During subsequent dynamical interactions, the eccentricities of Uranus and Neptune can exceed 0.5, and in 50% of simulation runs (including this), they exchange orbits. The maximum eccentricity over the last 2 Myr of evolution is indicated. From Tsiganis et al. (2005, Figure 1), by permission from Macmillan Publishers Ltd, Nature, ©2005.

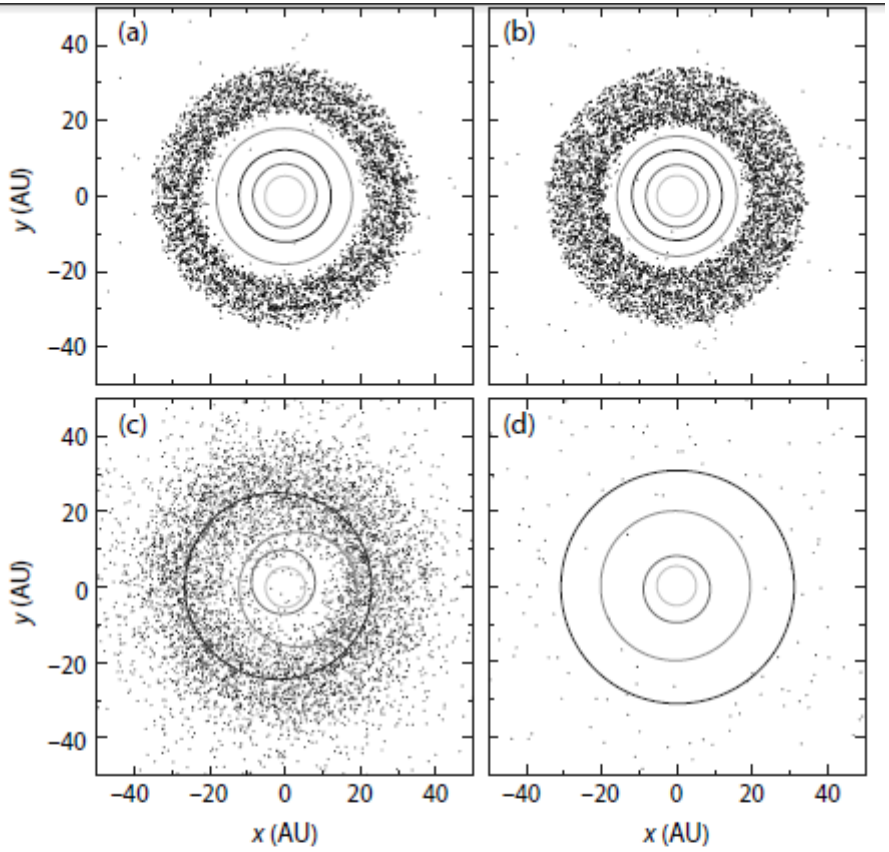

Figure 12.5: Numerical simulations of the lunar heavy bombardment. Planetary orbits and disk planetesimals are projected on the initial mean orbital plane. The four giant planets were initially on nearly circular coplanar orbits, with a = 5.45, 8.18, 11.5 and 14.2 AU, and the planetesimal disk, of total mass $35 M_{\oplus}$, extended from 15.5–34 AU. Panels represent the system at (a) the start of planetary migration (100 Myr); (b) just before the start of the lunar heavy bombardment (879 Myr); (c) just after its start (882 Myr); and (d) 200 Myr later when only 3% of the initial disk mass remains, and the planets have achieved their final orbits. From Gomes et al. (2005, Figure 2), by permission from Macmillan Publishers Ltd, Nature, ©2005.

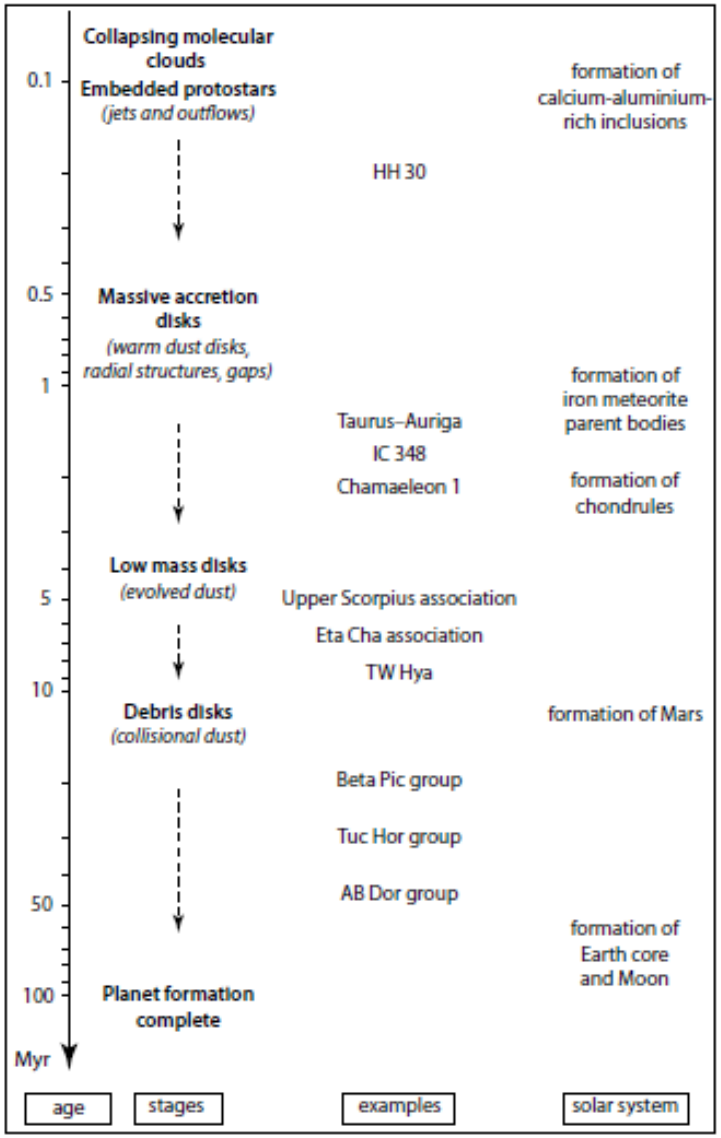

Figure 10.1: Chronology of the early stages of planet formation, from an arbitrary initial time, showing some of the main evolutionary stages, some representative astronomical examples, and some specific epochs relevant for the solar system (see also §12.5). The figure is an adaptation of a more detailed chronology given by Apai & Lauretta (2010, Figure 1.3).

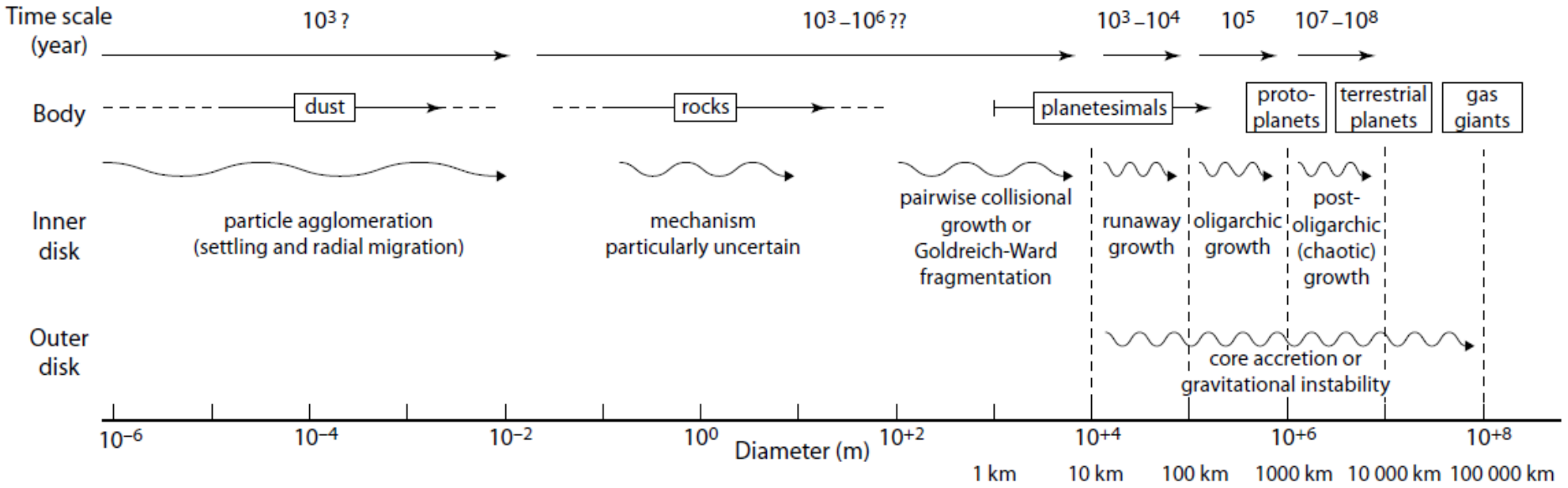

Figure 10.6: Schematic of the growth of planets, starting with sub-micron dust, and extending up to the terrestrial planets in the inner disk, and the gas giants in the outer disk. Some indicative time scales are given, although some intervals, especially around the meter-size barrier, remain highly uncertain.

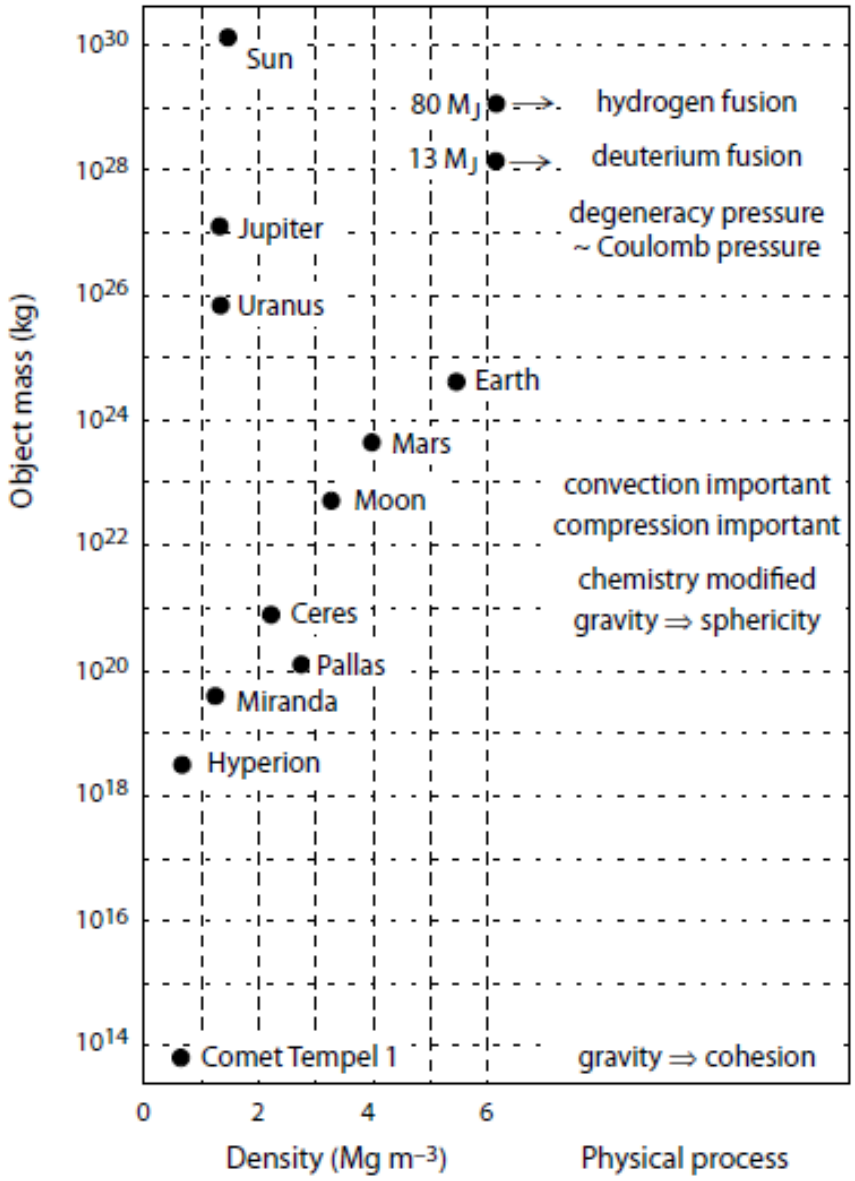

Figure 10.8: The effect of gravity on shape and structure as a function of mass. Some solar system objects are given as examples. The radii of brown dwarfs are approximately constant above ~ 13M_J, and their densities fall off the plot to the right.

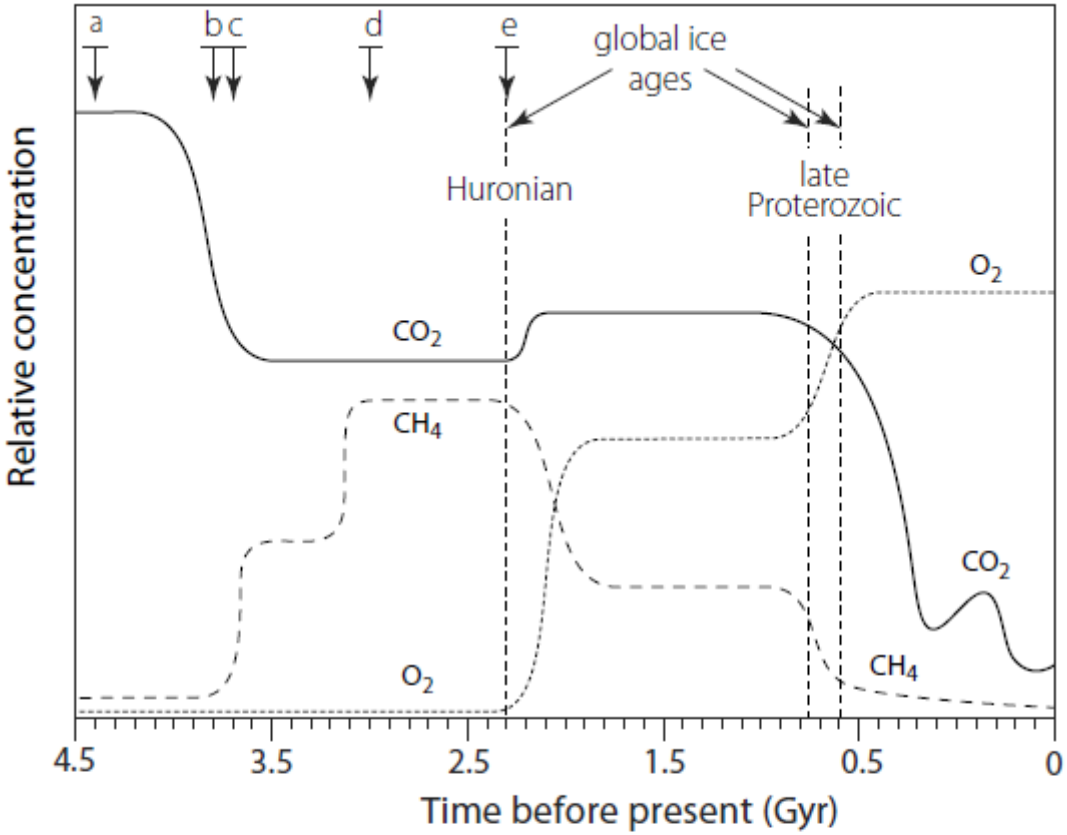

Figure 12.7: Relative concentrations of CO_2, CH_4, and O_2 over Earth's history. Key epochs are: (a) high concentrations of CO_2 compensate for the lower luminosity of the young Sun; (b) the first microscopic life begins consuming CO_2; (c) methanogens start to contribute to the atmosphere; (d) the appearance of O_2-producing bacteria; (e) the appearance of atmospheric O_2. The epoch of the origin of the CH_4-producing microbes is somewhat arbitrary. Adapted from Kasting (2004, Figure 3).

BIBLIOGRAFIA:

- The Exoplanet Handbook, Perryman
- Fundamental Planetary Science, Lissauer y de Pater
- Astrophysics of Planet Formation, Armitage